The Astronomical Journal, 168:49 (16pp), 2024 August https://doi.org/10.3847/1538-3881/ad4ce5

Systematic KMTNet Planetary Anomaly Search. XII. Complete Sample of 2017 Subprime Field Planets

Yuqian Gui[1], Weicheng Zang[1,2], Ruocheng Zhai[1], Yoon-Hyun Ryu[3], Andrzej Udalski[4], Hongjing Yang[1], Cheongho Han[5], Shude Mao[1,6]
(Leading Authors),
Michael D. Albrow[7], Sun-Ju Chung[8], Andrew Gould[9,10], Kyu-Ha Hwang[8], Youn Kil Jung[8,11], In-Gu Shin[2], Yossi Shvartzvald[12], Jennifer C. Yee[2], Sang-Mok Cha[8,13], Dong-Jin Kim[8], Hyoun-Woo Kim[8], Seung-Lee Kim[8], Chung-Uk Lee[8], Dong-Joo Lee[8], Yongseok Lee[8,13], Byeong-Gon Park[8], Richard W. Pogge[14,15]
(The KMTNet Collaboration),
Przemek Mróz[4], Michał K. Szymański[4], Jan Skowron[4], Radosław Poleski[4], Igor Soszyński[4], Paweł Pietrukowicz[4], Szymon Kozłowski[4], Krzysztof Ulaczyk[16], Krzysztof A. Rybicki[4,17], Patryk Iwanek[4], Marcin Wrona[4], Mariusz Gromadzki[4]
(The OGLE Collaboration),
and
Hanyue Wang[2], Jiyuan Zhang[1], Renkun Kuang[1,18], Qiyue Qian[1], and Wei Zhu[1]
(The MAP Collaboration)

[1] Department of Astronomy, Tsinghua University, Beijing 100084, People's Republic of China; 3130102785@zju.edu.cn
[2] Center for Astrophysics | Harvard & Smithsonian, 60 Garden St., Cambridge, MA 02138, USA
[3] Korea Astronomy and Space Science Institute, Daejon 34055, Republic of Korea
[4] Astronomical Observatory, University of Warsaw, Al. Ujazdowskie 4, 00-478 Warszawa, Poland
[5] Department of Physics, Chungbuk National University, Cheongju 28644, Republic of Korea
[6] National Astronomical Observatories, Chinese Academy of Sciences, Beijing 100101, People's Republic of China
[7] University of Canterbury, School of Physical and Chemical Sciences, Private Bag 4800, Christchurch 8020, New Zealand
[8] Korea Astronomy and Space Science Institute, Daejeon 34055, Republic of Korea
[9] Max-Planck-Institute for Astronomy, Königstuhl 17, 69117 Heidelberg, Germany
[10] Department of Astronomy, Ohio State University, 140 W. 18th Ave., Columbus, OH 43210, USA
[11] National University of Science and Technology (UST), Daejeon 34113, Republic of Korea
[12] Department of Particle Physics and Astrophysics, Weizmann Institute of Science, Rehovot 7610001, Israel
[13] School of Space Research, Kyung Hee University, Yongin, Kyeonggi 17104, Republic of Korea
[14] Department of Astronomy, Ohio State University, 140 West 18th Ave., Columbus, OH 43210, USA
[15] Center for Cosmology and AstroParticle Physics, Ohio State University, 191 West Woodruff Ave., Columbus, OH 43210, USA
[16] Department of Physics, University of Warwick, Gibbet Hill Rd., Coventry CV4 7AL, UK
[17] Department of Particle Physics and Astrophysics, Weizmann Institute of Science, Rehovot 76100, Israel
[18] Department of Engineering Physics, Tsinghua University, Beijing 100084, People's Republic of China
Received 2024 April 13; revised 2024 May 7; accepted 2024 May 15; published 2024 July 2

Abstract

We report the analysis of four unambiguous planets and one possible planet from the subprime fields ($\Gamma \leqslant 1\ \mathrm{hr}^{-1}$) of the 2017 Korea Microlensing Telescope Network (KMTNet) microlensing survey, to complete the KMTNet AnomalyFinder planetary sample for the 2017 subprime fields. They are KMT-2017-BLG-0849, KMT-2017-BLG-1057, OGLE-2017-BLG-0364, and KMT-2017-BLG-2331 (unambiguous), as well as KMT-2017-BLG-0958 (possible). For the four unambiguous planets, the mean planet–host mass ratios, q, are $(1.0, 1.2, 4.6, 13) \times 10^{-4}$, the median planetary masses are $(6.4, 24, 76, 171)\ M_{\oplus}$, and the median host masses are $(0.19, 0.57, 0.49, 0.40)\ M_{\odot}$, respectively, found from a Bayesian analysis. We have completed the Anomaly Finder planetary sample from the first 4 yr of KMTNet data (2016–2019), with 112 unambiguous planets in total, which nearly tripled the microlensing planetary sample. The "sub-Saturn desert" ($\log q = [-3.6, -3.0]$) found in the 2018 and 2019 KMTNet samples is confirmed by the 2016 and 2017 KMTNet samples.

Unified Astronomy Thesaurus concepts: Gravitational microlensing exoplanet detection (2147); Gravitational microlensing (672)

1. Introduction

The gravitational microlensing technique is most sensitive to planets around or beyond Jupiter-like orbits (Mao & Paczynski 1991; Gould & Loeb 1992; Bennett & Rhie 1996; Gaudi 2012; Mao 2012). Since 2016, The Korea Microlensing Telescope Network (KMTNet; Kim et al. 2016) has been conducting a microlensing survey toward the Galactic bulge to search for

Table 1
Event Names, Alert, Locations, and Cadences for the Seven Events Analyzed in this Paper

Event Name	First Alert Date	R.A. (J2000)	Decl. (J2000)	ℓ	b	Cadence
KMT-2017-BLG-0849	Postseason	17:41:26.27	−25:16:52.39	+2.6253	+2.7087	0.4 hr^{-1}
KMT-2017-BLG-1057	Postseason	17:41:56.64	−22:20:06.40	+5.1968	+4.1592	0.4 hr^{-1}
OGLE-2017-BLG-0364	2017 Mar 20	17:40:54.69	−34:37:03.3	−5.3617	−2.1315	0.5–1 per night
KMT-2017-BLG-1396						0.4 hr^{-1}
KMT-2017-BLG-2331	Postseason	17:37:37.73	−29:27:40.36	−1.3672	+1.2033	1.0 hr^{-1}
KMT-2017-BLG-0958	Postseason	17:48:46.65	−25:44:31.20	+3.0954	+1.0553	1.0 hr^{-1}

microlensing planets. The advent of KMTNet has played a major or decisive role in about 70% of published microlensing planetary discoveries.[19] Before 2021, most KMTNet planets were found using by-eye searches and published without a systematic approach. That is, most planetary detection papers did not have a strong connection with others and were published by a systematic approach based on the planets' similar properties, such as mass ratios, observing seasons, or cadences. A disadvantage of this approach is the difficulty to form a large-scale ($\mathcal{O}(10^2)$) homogeneous planetary sample for statistical studies.

The KMTNet AnomalyFinder (Zang et al. 2021b, 2022b) adopted the KMTNet EventFinder algorithm (Gould 1996; Kim et al. 2018) to search for anomalies from the residuals to a point-source point–lens (PSPL; Paczyński 1986) model. The initial motivation of Zang et al. (2021b) for building AnomalyFinder is to solve the "missing planetary caustics" problem in the KMTNet planetary sample, and later Zang et al. (2021b) realized that AnomalyFinder can also be a new pathway toward a large-scale homogeneous KMTNet planetary sample, besides high-magnification planetary samples from the KMTNet data only (Yee et al. 2021) and follow-up observations (Zang et al. 2021a). Then, a systematic search based on AnomalyFinder, followed by systematic analyses and publications, was conducted with the 2016–2019 KMTNet data.

In total, KMTNet monitors ∼97 deg^2 of the Galactic bulge area, including the ∼13 deg^2 prime fields with cadences of $\Gamma \geqslant 2$ hr^{-1} and the ∼84 deg^2 subprime fields with cadences of $\Gamma \leqslant 1$ hr^{-1}. See Figure 12 of Kim et al. (2018) for the field locations and cadences. Prior to the construction of a complete sample for the 2017 subprime fields, which is the subject of the present work, complete samples had previously been constructed for the 2019 prime fields (Zang et al. 2021b, 2022b; Hwang et al. 2022), the 2019 subprime fields (Jung et al. 2023), the 2018 prime fields (Gould et al. 2022; Hwang et al. 2022; Wang et al. 2022), the 2018 subprime fields (Jung et al. 2022), the 2017 prime fields (Ryu et al. 2024), the 2016 prime fields (Shin et al. 2023), the 2016 subprime fields (Shin et al. 2024), as well as all remaining KMTNet planets with a planet–host mass ratio $q < 10^{-4}$ (Zang et al. 2023) from 2016 to 2019. The above references are (ignoring duplicates) Papers I, II, IV, VI, V, III, VI, X, IX, XI, and VII in the AnomalyFinder paper series. In addition, based on the $\log q > -4$ AnomalyFinder planets from the 2018 and 2019 seasons and the $\log q < -4$ AnomalyFinder planets from the 2016 to 2019 seasons, Zang et al. (2024) formed a homogeneously selected statistical sample and studied the KMTNet planetary mass-ratio function.

[19] http://exoplanetarchive.ipac.caltech.edu as of 2024 February 13.

For this paper, we present the complete sample of the 2017 subprime-field sample, which is the twelfth paper of the AnomalyFinder paper series. From the 2017 KMTNet subprime data, the AnomalyFinder algorithm found 3315 candidate signals, and the operator (W. Zang) identified 133 anomalous events. Of them, 10 were already published using by-eye searches, including six unambiguous planets (Calchi Novati et al. 2018; Shin et al. 2019a; Han et al. 2021, 2022), two planet candidates consisting of binary-lens single-source/single-lens binary-source (2L1S/1L2S; Gaudi 1998) degeneracy (Shin et al. 2019a), and two finite-source point–lens (Gould 1994; Nemiroff & Wickramasinghe 1994; Witt & Mao 1994) events (Shvartzvald et al. 2019; Han et al. 2020). For the remaining events, detailed light-curve analysis shows that 14 are potentially planetary with $q_{\rm online} < 0.05$, where $q_{\rm online}$ is the mass ratio from a fitting to the online data. We further investigate them with the "tender-loving care" rereduction photometry from a careful check on the reference images and other parameters of the photometric pipeline. See Yang et al. (2024) for an example. We find that two are clear stellar-binary events, 10 are unambiguous planetary events, one is a 2L1S/1L2S event (Y. Gui et al. 2024, in preparation), and one is a candidate planetary event with a stellar-binary alternate interpretation. Zang et al. (2023) has published three of the unambiguous planetary events, while three unambiguous planetary events, OGLE-2017-BLG-1630/MOA-2017-BLG-441/KMT-2017-BLG-1237, OGLE-2017-BLG-0668/KMT-2017-BLG-1145, and KMT-2017-BLG-2197 will be published elsewhere. Here we introduce a detailed analysis of the four remaining unambiguous planetary events and the candidate planetary event.

2. Observations

Table 1 shows the basic observational information for the seven events, including the event names, the first alert dates, event coordinates in the equatorial and Galactic systems, and the observing cadences from the different groups. The event names are in order of the discovery date and we designate them by their first discovery names.

The observations of KMTNet were conducted by its three identical 1.6 m telescopes equipped with 4 deg^2 cameras in Chile (KMTC), South Africa (KMTS), and Australia (KMTA). The Optical Gravitational Lensing Experiment (OGLE) took data using one 1.3 m telescope equipped with a 1.4 deg^2 camera in Chile (Udalski et al. 2015). The event, OGLE-2017-BLG-0364, was first discovered by the Early Warning System of OGLE (Udalski et al. 1994; Udalski 2003), and all of the five events were found by the KMTNet postseason EventFinder algorithm (Kim et al. 2018). Most KMTNet and OGLE images

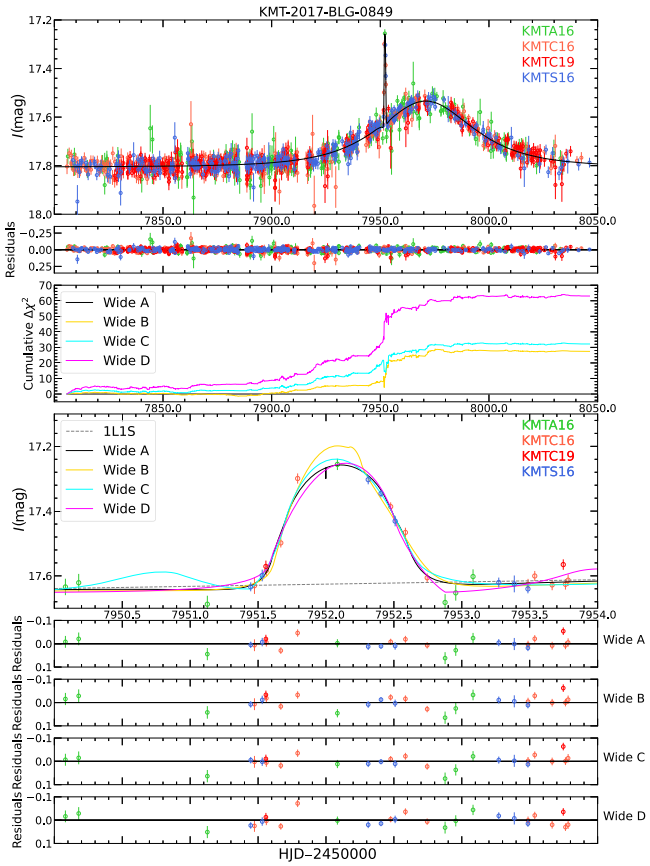

Figure 1. Observed data and the 2L1S wide (the solid black, yellow, cyan, and magenta lines) and 1L1S models (the dashed gray line) for KMT-2017-BLG-0849 and its bump-type anomaly. Different data sets are shown with different colors. The third panel shows the cumulative $\Delta\chi^2$ distribution of models relative to the Wide A model.

were taken in the *I*-band filter, and a fraction of *V*-band images were acquired for source color measurements. To the best of our knowledge, there were no follow-up observations for any of these events, and this is certainly the case for the four events with KMTNet names.

KMT-2017-BLG-0849 was located in two overlapping KMTNet fields, BLG16 and BLG19, but at the edge of the BLG19 images, so only a few KMTC19 data points are useful and the effective observing cadence is still the cadence of the BLG16 field, i.e., 0.4 hr^{-1}.

The data used in the light-curve analysis were reduced using a difference imaging analysis (DIA; Tomaney & Crotts 1996; Alard & Lupton 1998) as implemented by each group: Albrow et al. (2009) and Yang et al. (2024) for KMTNet and Wozniak (2000) for OGLE. The photometric error bars estimated by the DIA pipelines were recalibrated using the method outlined by Yee et al. (2012), which enables the χ^2 value per degree of freedom (dof) for each data set to unity.

3. Light-curve Analysis

3.1. Preamble

We conduct the light-curve analysis in this section, following the procedures of Zang et al. (2023). To avoid redundant descriptions, we introduce the definitions of the parameter symbols here. We refer the reader to Zang et al. (2023) for more details.

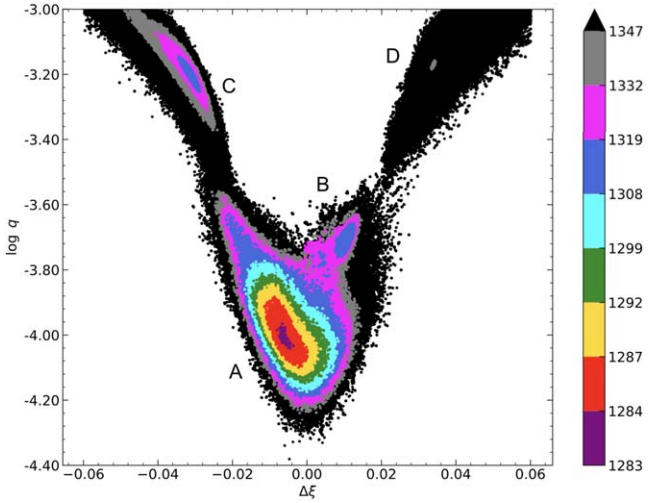

Figure 2. Scatterplot of the hotter MCMC of $\Delta\xi$ vs. $\log q$ of KMT-2017-BLG-0849, where $\Delta\xi$ is the offset between the center of the caustic and the intersection of the source trajectory and the planet–host axis. We find $\Delta\chi^2$ barriers of ∼20 between the Wide A and Wide B models, ∼70 between the Wide A and Wide C models, and $\Delta\chi^2 \sim 90$ between the Wide B and Wide D models. The respectively color coding is purple, red, yellow, green, cyan, blue, magenta, and gray for $\Delta\chi^2 < (1, 4, 9, 16, 25, 36, 49, 64)$. We use black dots to symbolize $\Delta\chi^2 > 64$.

All of the events are fitted by static 2L1S models, which have seven parameters, including the three PSPL parameters (t_0, u_0, t_E), i.e., the time of the closest lens–source approach, the impact parameter in units of the angular Einstein radius θ_E, and the Einstein timescale

$$t_\mathrm{E} = \frac{\theta_\mathrm{E}}{\mu_\mathrm{rel}}, \qquad \theta_\mathrm{E} = \sqrt{\kappa M_\mathrm{L} \pi_\mathrm{rel}}, \tag{1}$$

where $\kappa \equiv \dfrac{4G}{c^2 \mathrm{au}} \simeq 8.144 \dfrac{\mathrm{mas}}{M_\odot}$, M_L is the mass of the lens system and (π_rel, μ_rel) are the lens–source relative (parallax, proper motion). Three parameters describe the binary geometry (s, q, α), i.e., the planet–host projected separation scaled to θ_E, the planet–host mass ratio, and the angle between the source trajectory and the binary axis. The last parameter, ρ, denotes the ratio of the angular source radius, θ_*, to θ_E, i.e., $\rho = \theta_*/\theta_\mathrm{E}$.

We use the advanced contour integration code `VBBinaryLensing` (Bozza 2010; Bozza et al. 2018) to compute the magnification of 2L1S models, $A(t)|_{(t_0,u_0,t_\mathrm{E},\rho,q,s,\alpha)}$, at any given time t. For each data set i, we introduce two linear flux parameters, $f_{\mathrm{S},i}$ and $f_{\mathrm{B},i}$, to represent the flux of the source star and any blend flux, respectively. Then, the observed flux, $f_i(t)$, is modeled as

$$f_i(t) = f_{\mathrm{S},i} A(t)|_{(t_0,u_0,t_\mathrm{E},\rho,q,s,\alpha)} + f_{\mathrm{B},i}. \tag{2}$$

We first conduct a grid search with fixed ($\log q$, $\log s$, ρ) and (t_0, u_0, t_E, α) allowed to vary. We adopt uniform priors for (t_0, u_0, t_E, $\log\rho$, α, $\log s$, $\log q$). We explore the models by Markov Chain Monte Carlo (MCMC) χ^2 minimization using the `emcee` ensemble sampler (Foreman-Mackey et al. 2013) and then search for the minimum χ^2 by a downhill approach with the `SciPy` package (Virtanen et al. 2020). Then, we refine one or more local minima with all parameters free. During the fitting, $f_{\mathrm{S},i}$ and $f_{\mathrm{B},i}$ are not MCMC parameters and are derived by linear regression. The fitting parameter values shown below are the medians and 68% equal-tail intervals of the marginal posterior distribution.

Table 2
Lensing Parameters for KMT-2017-BLG-0849

Parameters	2L1S						1L2S
	Wide A	Wide B	Wide C	Wide D	Close Outer	Close Inner	
χ^2/dof	**1283.6/1301**	1310.7/1301	1315.6/1301	1346.3/1301	1502.2/1301	1603.5/1301	1554.2/1301
$t_{0,1}$ (HJD′)	**7970.95**$^{+0.19}_{-0.18}$	7970.95$^{+0.18}_{-0.18}$	7970.75$^{+0.18}_{-0.19}$	7970.75$^{+0.19}_{-0.19}$	7971.02$^{+0.19}_{-0.18}$	7970.87$^{+0.18}_{-0.19}$	7972.18$^{+0.20}_{-0.17}$
$t_{0,2}$ (HJD′)							7952.14$^{+0.01}_{-0.01}$
$u_{0,1}$	**1.00**$^{+0.06}_{-0.07}$	0.67$^{+0.03}_{-0.03}$	0.60$^{+0.03}_{-0.03}$	0.47$^{+0.01}_{-0.01}$	0.53$^{+0.03}_{-0.03}$	1.11$^{+0.03}_{-0.03}$	0.68$^{+0.17}_{-0.12}$
$u_{0,2}$ (10^{-3})							$-0.05^{+0.66}_{-0.68}$
$t_{\rm E}$ (days)	**26.4**$^{+1.4}_{-1.1}$	34.0$^{+1.1}_{-0.9}$	37.2$^{+1.3}_{-1.1}$	44.1$^{+0.9}_{-0.9}$	40.8$^{+1.5}_{-1.4}$	24.5$^{+0.6}_{-0.5}$	32.8$^{+4.5}_{-4.6}$
ρ_1 (10^{-2})	**1.76**$^{+0.10}_{-0.11}$	0.86$^{+0.08}_{-0.08}$	1.06$^{+0.04}_{-0.04}$	0.87$^{+0.03}_{-0.03}$	0.34$^{+0.02}_{-0.02}$	1.53$^{+0.07}_{-0.19}$	
ρ_2 (10^{-2})							1.09$^{+0.17}_{-0.13}$
$q_{f,I}$ (10^{-3})							5.5$^{+1.2}_{-1.2}$
α (rad)	**4.095**$^{+0.012}_{-0.013}$	4.021$^{+0.011}_{-0.012}$	4.016$^{+0.012}_{-0.012}$	3.978$^{+0.010}_{-0.010}$	0.763$^{+0.012}_{-0.012}$	1.063$^{+0.008}_{-0.008}$	
s	**1.79**$^{+0.05}_{-0.06}$	1.52$^{+0.02}_{-0.02}$	1.48$^{+0.02}_{-0.02}$	1.34$^{+0.01}_{-0.01}$	0.71$^{+0.01}_{-0.01}$	0.53$^{+0.01}_{-0.01}$	
q(10^{-4})	**1.01**$^{+0.15}_{-0.11}$	1.95$^{+0.09}_{-0.09}$	6.33$^{+0.49}_{-0.42}$	6.73$^{+0.32}_{-0.32}$	8.81$^{+0.63}_{-0.59}$	15.58$^{+1.27}_{-2.11}$	
$\log q$	**−3.996**$^{+0.061}_{-0.052}$	−3.711$^{+0.019}_{-0.021}$	−3.199$^{+0.032}_{-0.030}$	−3.172$^{+0.020}_{-0.021}$	−3.055$^{+0.030}_{-0.030}$	−2.807$^{+0.034}_{-0.063}$	
$f_{\rm S,KMTC}$	**1.01**$^{+0.14}_{-0.14}$	0.48$^{+0.03}_{-0.04}$	0.39$^{+0.03}_{-0.03}$	0.27$^{+0.01}_{-0.01}$	0.32$^{+0.03}_{-0.02}$	1.27$^{+0.08}_{-0.08}$	0.48$^{+0.24}_{-0.13}$
$f_{\rm B,KMTC}$	**0.19**$^{+0.14}_{-0.14}$	0.71$^{+0.04}_{-0.03}$	0.80$^{+0.03}_{-0.03}$	0.92$^{+0.01}_{-0.01}$	0.87$^{+0.02}_{-0.03}$	−0.07$^{+0.08}_{-0.08}$	0.72$^{+0.13}_{-0.24}$

Note. All fluxes are on an 18th magnitude scale, e.g., $I_{\rm S} = 18 - 2.5\log(f_{\rm S})$. The bold font indicates the best-fit model.

In some cases, we also investigate whether the microlensing parallax vector (Gould 1992, 2000, 2004)

$$\boldsymbol{\pi}_{\rm E} \equiv \frac{\pi_{\rm rel}}{\theta_{\rm E}} \frac{\boldsymbol{\mu}_{\rm rel}}{\mu_{\rm rel}}, \tag{3}$$

can be usefully constrained by the data. We fit it by two parameters, $\boldsymbol{\pi}_{\rm E,N}$ and $\boldsymbol{\pi}_{\rm E,E}$, the north and east components of the microlensing parallax vector, respectively, in equatorial coordinates. We also consider the lens orbital motion effect (Batista et al. 2011; Skowron et al. 2011) when including the microlensing parallax and fit the $u_0 > 0$ and $u_0 < 0$ solutions for the "ecliptic degeneracy" (Jiang et al. 2004; Poindexter et al. 2005).

In cases without sharp caustic-crossing features, we also check 1L2S models because 2L1S models can be mimicked by 1L2S models (Gaudi 1998). For a static 1L2S model, the total effective magnification at wave band λ, $A_\lambda(t)$, can be expressed as (Hwang et al. 2013)

$$A_\lambda(t) = \frac{A_1(t) f_{{\rm S},1,\lambda} + A_2(t) f_{{\rm S},2,\lambda}}{f_{{\rm S},1,\lambda} + f_{{\rm S},2,\lambda}} = \frac{A_1(t) + q_{f,\lambda} A_2(t)}{1 + q_{f,\lambda}}, \tag{4}$$

$$q_{f,\lambda} = \frac{f_{{\rm S},2,\lambda}}{f_{{\rm S},1,\lambda}}, \tag{5}$$

where $f_{{\rm S},j,\lambda}$ represents the source flux at wave band λ, $A_j(t)$ represents magnification of each source, $q_{f,\lambda}$ is the flux ratio between the secondary and the primary sources, and $j = 1$ and $j = 2$ correspond to the primary and the secondary sources, respectively.

Zang et al. (2024) considered a model as a degenerate model if it has $\Delta\chi^2 < 10$ compared to the best-fit model, and several papers in the AnomalyFinder paper series also adopted this criterion (e.g., Shin et al. 2023). For the present paper, we adopt a loose criterion to exclude a model with $\Delta\chi^2 > 20$. Because we will provide $\Delta\chi^2$ for each model, one can easily test different criteria when forming a planetary sample.

3.2. KMT-2017-BLG-0849

Figure 1 displays the light curve of KMT-2017-BLG-0849. The light curve exhibits a bump-type anomaly, which could, in principle, be caused by a 2L1S or a 1L2S model. We first consider the 2L1S modeling. By excluding the data over the anomaly, a PSPL fit yields $(t_0, u_0, t_{\rm E}) = (7971.2, 1.10, 24.9)$. From Figure 1, the anomaly occurred at $t_{\rm anom} = 7952.1$, corresponding to a lens–source offset (in units of $\theta_{\rm E}$) of

$$u_{\rm anom} = \sqrt{u_0^2 + \left(\frac{t_{\rm anom} - t_0}{t_{\rm E}}\right)^2} = 1.34, \tag{6}$$

and

$$|\alpha| = \left| \sin^{-1} \frac{u_0}{u_{\rm anom}} \right| = 0.96 \text{ rad}. \tag{7}$$

Because the planetary caustics are located at the position of $|s - s^{-1}| \sim u_{\rm anom}$, we obtain

$$s_\pm \sim \frac{\sqrt{u_{\rm anom}^2 + 4} \pm u_{\rm anom}}{2}, \tag{8}$$

where $s = s_+ = 1.87$ and $s = s_- = 0.53$ respectively represent the major-image and minor-image planetary caustics, and we define them as wide and close topology, respectively.

We first analyze the wide topology. The bump-type anomaly exhibits strong finite-source effects, so the planetary caustic may be fully enveloped by a large source. According to the PSPL model and Figure 1, the excess magnification of the anomaly is 0.63. Gould & Gaucherel (1997) showed that the excess magnification can be estimated by

$$\Delta A = \frac{2q}{\rho^2}. \tag{9}$$

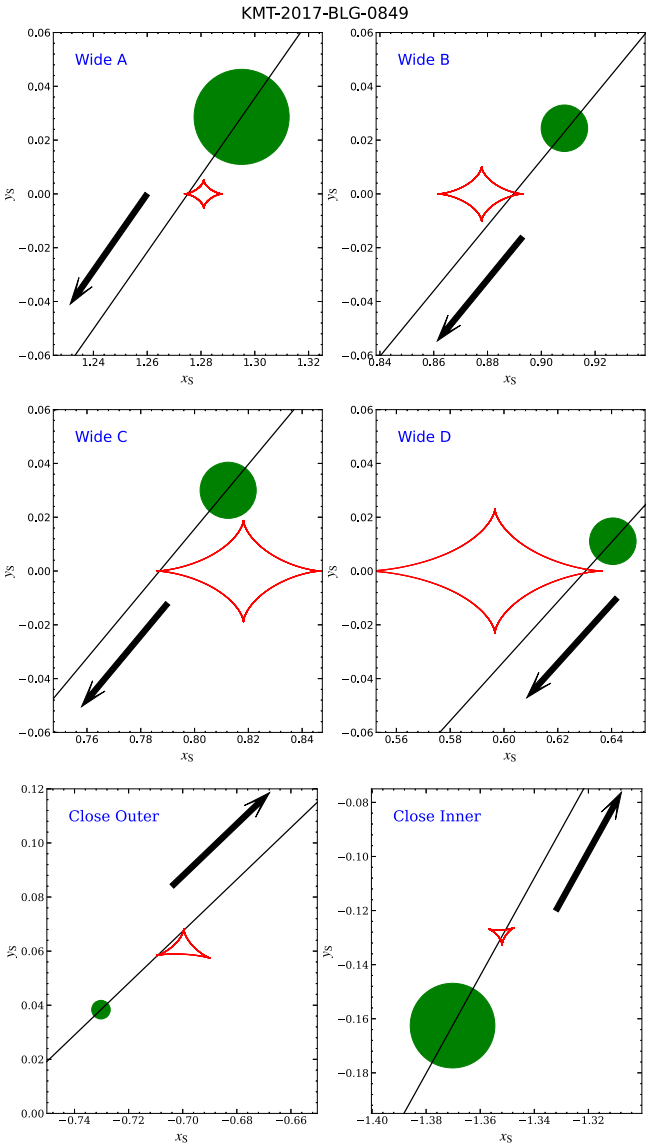

Figure 3. Caustic-crossing geometries of KMT-2017-BLG-0849 models. In each panel, the red lines represent the caustics, the solid black line represents the source trajectory, the radius of the green dot represents the source radius, and the line with an arrow indicates the direction of the source motion.

We estimate ρ using the duration of the FWHM of the bump, $t_{\rm fwhm} \sim 0.8$ days, and get

$$\rho \sim \frac{t_{\rm fwhm}}{2t_{\rm E}} \sim 0.016. \quad (10)$$

Then, we obtain

$$q = \frac{\Delta A \rho^2}{2} = 8.1 \times 10^{-5}. \quad (11)$$

We expect that ρ and q are lower limits because the caustic-crossing time is $\leqslant 2t_{\rm E}\rho$ for a larger source. We use the parameters obtained from the estimation above as the MCMC initial guess.

For such a bump-type anomaly in a low-magnification event, the wide topology could have several local minima (e.g., Hwang et al. 2018; Zang et al. 2022a). Therefore, we investigate the wide topology by a "hotter" MCMC by multiplying all photometric error bars by a factor of 3.0 during the MCMC. We introduce the

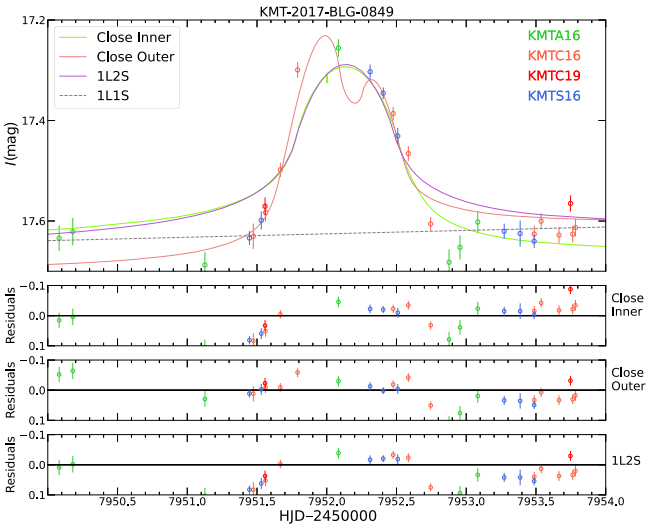

Figure 4. A close-up of the anomaly with the 2L1S close and 1L2S models of KMT-2017-BLG-0849. The symbols are similar to those in Figure 1.

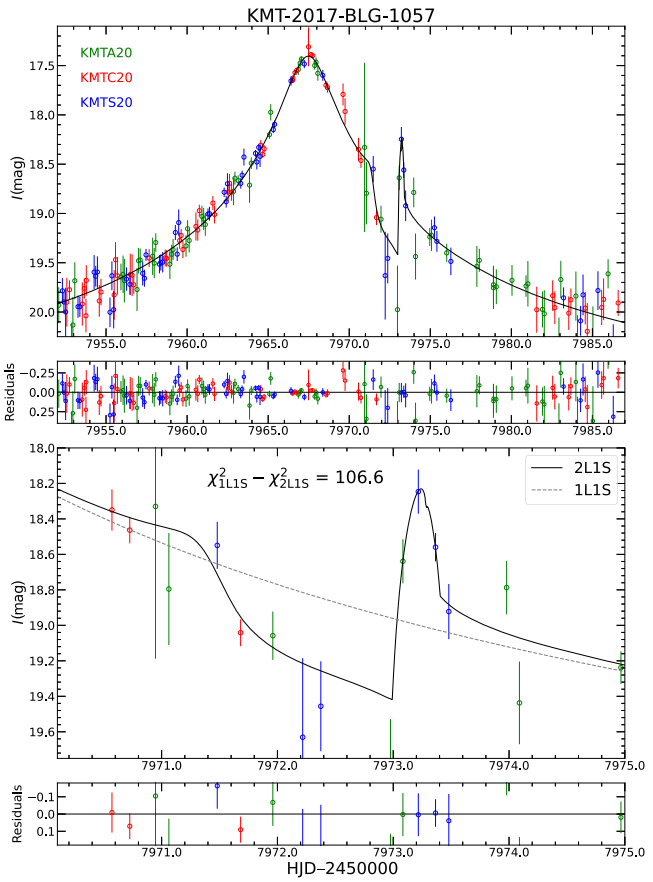

Figure 5. Observed data and the 2L1S model for KMT-2017-BLG-1057. The symbols are similar to those in Figure 1.

offset between the source and the planetary caustic as the source crosses the binary axis (Hwang et al. 2018)

$$\Delta\xi = u_0 \csc(\alpha) - (s - s^{-1}). \quad (12)$$

Figure 2 shows a $\Delta\xi$ versus $\log q$ scatterplot for the resulting MCMC by multiplying the resulting χ^2 by 9. We find four local minima and then refine all of them. We label them as "Wide A," "Wide B," "Wide C," and "Wide D" based on $s > 1$.

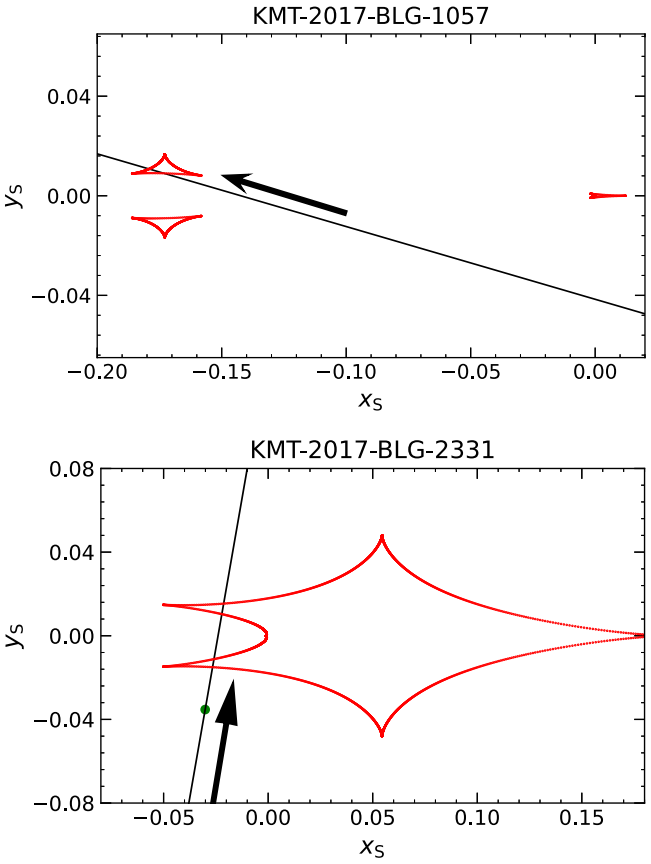

Figure 6. Geometries of the KMT-2017-BLG-1057 and KMT-2017-BLG-2331 models. The symbols are similar to those in Figure 3.

Table 3
2L1S Parameters for Two Events

Parameters	KMT-2017-BLG-1057	KMT-2017-BLG-2331
χ^2/dof	805.29/805	257.84/258
t_0 (HJD′)	$7967.49^{+0.03}_{-0.02}$	$8006.11^{+0.03}_{-0.03}$
u_0	$0.039^{+0.003}_{-0.003}$	$0.024^{+0.003}_{-0.002}$
t_E (days)	$33.83^{+2.23}_{-2.27}$	$48.09^{+3.06}_{-2.91}$
ρ (10^{-3})	<2.5	$2.04^{+0.32}_{-0.26}$
α (rad)	$2.86^{+0.01}_{-0.01}$	$1.41^{+0.03}_{-0.03}$
s	$0.918^{+0.005}_{-0.004}$	$1.030^{+0.012}_{-0.010}$
q(10^{-4})	$1.15^{+0.27}_{-0.18}$	$12.8^{+1.4}_{-1.1}$
$\log q$	$-3.937^{+0.091}_{-0.076}$	$-2.893^{+0.045}_{-0.040}$
$f_{S,KMTC}$	$0.068^{+0.006}_{-0.005}$	$0.014^{+0.001}_{-0.001}$
$f_{B,KMTC}$	$0.012^{+0.005}_{-0.005}$	$0.187^{+0.001}_{-0.001}$

Note. The upper limit on ρ is 3σ.

Table 2 presents the parameters for the four models, Figure 1 shows their best-fit light curves, and Figure 3 exhibits their caustic-crossing geometries. We find that the Wide A and Wide C models cross the caustic on the left side, while the Wide B and Wide D models cross the right side. The four models follow the "Cannae"/"von Schlieffen" degeneracy for caustic crossing (Gaudi & Gould 1997; Hwang et al. 2018). That is, for the Wide A model the source fully envelops the planetary caustic (i.e., "Cannae"), and for the other three models only one flank of the caustic is enveloped (i.e., "von Schlieffen"). In addition, for the Wide C and Wide D models the source interacts with two ridges of the caustic separately, resulting in a small bump that abuts the observed anomaly.

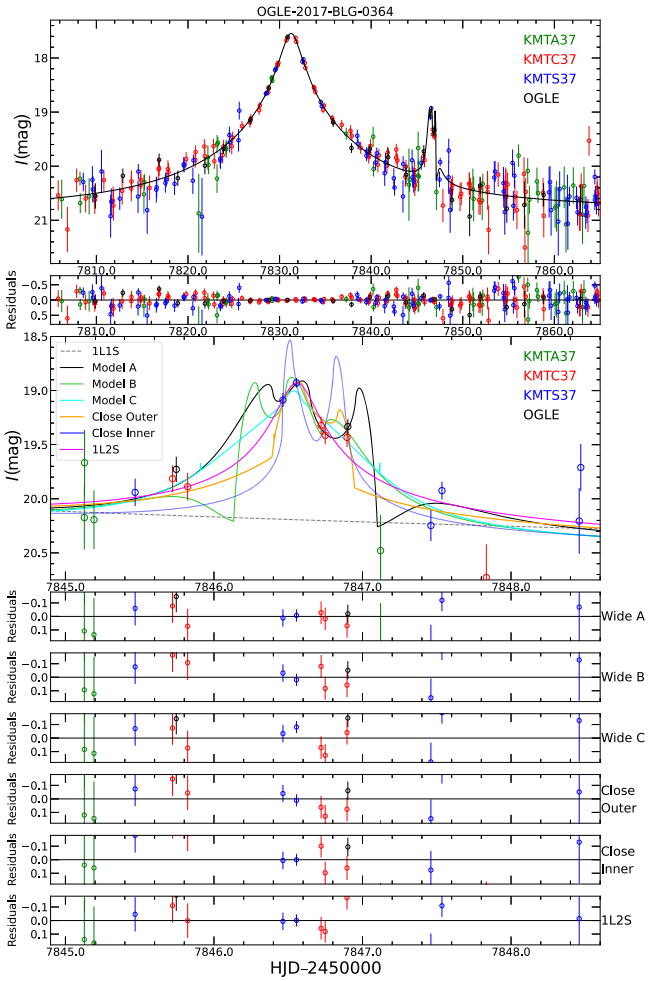

Figure 7. The observed data and the 2L1S and 1L2S models of OGLE-2017-BLG-0364.

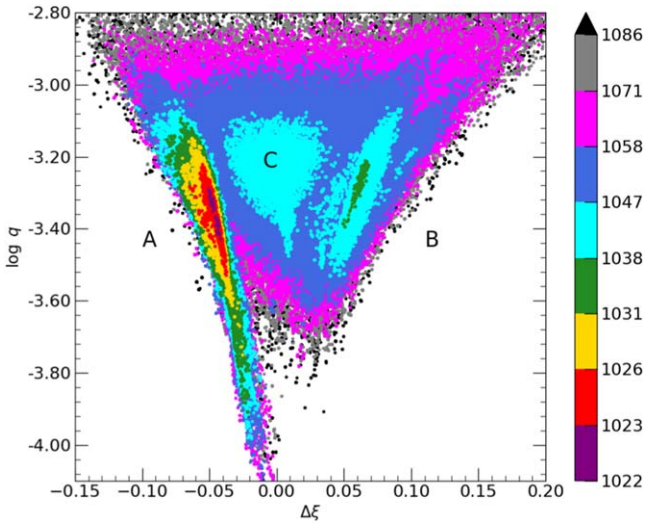

Figure 8. Scatterplot of the hotter MCMC of $\Delta\xi$ vs. $\log q$ for the wide models of OGLE-2017-BLG-0364. The distribution is derived by multiplying the photometric error bars by a factor of $\sqrt{3}$ and then multiplying the resulting χ^2 by 3.0 for the plot. We find three local minima and their parameters are provided in Table 4. The symbols are similar to those in Figure 2.

Table 4
Lensing Parameters for OGLE-2017-BLG-0364

Parameters	2L1S					1L2S
	Wide A	Wide B	Wide C	Close Outer	Close Inner	
χ^2/dof	**1021.8/1022**	1036.7/1022	1041.8/1022	1049.0/1022	1040.7/1022	1054.5/1022
$t_{0,1}$ (HJD′)	$\mathbf{7831.27}^{+0.02}_{-0.02}$	$7831.28^{+0.02}_{-0.02}$	$7831.28^{+0.02}_{-0.02}$	$7831.24^{+0.02}_{-0.02}$	$7831.24^{+0.02}_{-0.02}$	$7831.26^{+0.02}_{-0.02}$
$t_{0,2}$ (HJD′)						$7846.56^{+0.02}_{-0.02}$
$u_{0,1}$	$\mathbf{0.057}^{+0.002}_{-0.002}$	$0.069^{+0.003}_{-0.004}$	$0.072^{+0.003}_{-0.003}$	$0.047^{+0.002}_{-0.002}$	$0.055^{+0.002}_{-0.002}$	$0.067^{+0.006}_{-0.006}$
$u_{0,2}$						$0.009^{+0.001}_{-0.001}$
$t_{\rm E}$ (days)	$\mathbf{18.6}^{+0.6}_{-0.4}$	$15.9^{+0.7}_{-0.5}$	$15.6^{+0.5}_{-0.5}$	$22.9^{+0.7}_{-0.7}$	$19.3^{+0.3}_{-0.2}$	$16.4^{+1.1}_{-1.0}$
ρ_1 (10^{-2})	$\mathbf{0.20}^{+0.03}_{-0.03}$	$0.31^{+0.07}_{-0.07}$	$1.13^{+0.21}_{-0.28}$	$0.18^{+0.03}_{-0.04}$	$0.10^{+0.05}_{-0.02}$	
ρ_2 (10^{-2})						<1.9
$q_{f,I}$ (10^{-3})						$25.7^{+2.7}_{-2.2}$
α (rad)	$\mathbf{6.211}^{+0.001}_{-0.002}$	$6.215^{+0.002}_{-0.001}$	$6.211^{+0.002}_{-0.003}$	$2.951^{+0.008}_{-0.009}$	$3.174^{+0.003}_{-0.002}$	
s	$\mathbf{1.506}^{+0.015}_{-0.018}$	$1.585^{+0.022}_{-0.030}$	$1.603^{+0.024}_{-0.022}$	$0.718^{+0.007}_{-0.008}$	$0.679^{+0.003}_{-0.004}$	
$q(10^{-4})$	$\mathbf{4.64}^{+0.75}_{-0.76}$	$5.18^{+1.16}_{-0.92}$	$6.05^{+1.22}_{-1.01}$	$17.12^{+2.89}_{-2.06}$	$13.96^{+0.97}_{-0.81}$	
$\log q$	$\mathbf{-3.334}^{+0.065}_{-0.078}$	$-3.286^{+0.088}_{-0.085}$	$-3.218^{+0.080}_{-0.079}$	$-2.767^{+0.068}_{-0.056}$	$-2.855^{+0.029}_{-0.026}$	
$f_{\rm S,KMTC}$	$\mathbf{0.087}^{+0.002}_{-0.003}$	$0.106^{+0.004}_{-0.006}$	$0.109^{+0.005}_{-0.004}$	$0.070^{+0.003}_{-0.003}$	$0.084^{+0.002}_{-0.002}$	$0.103^{+0.009}_{-0.008}$
$f_{\rm B,KMTC}$	$\mathbf{-0.009}^{+0.003}_{-0.002}$	$-0.027^{+0.006}_{-0.004}$	$-0.030^{+0.004}_{-0.004}$	$0.007^{+0.003}_{-0.002}$	$-0.005^{+0.002}_{-0.002}$	$-0.026^{+0.008}_{-0.008}$

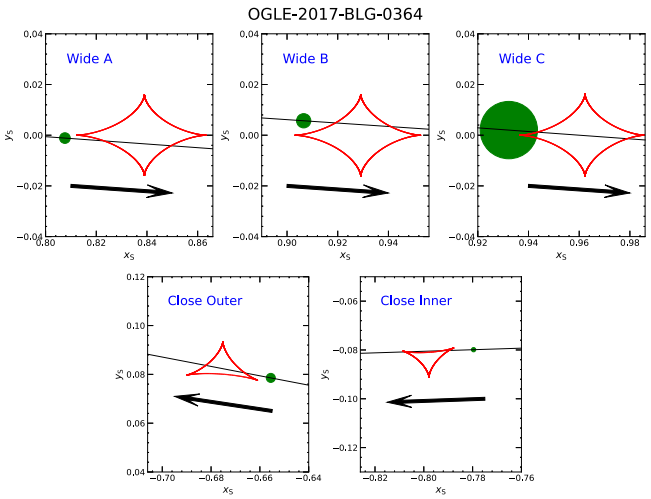

Figure 9. Caustic-crossing geometries of OGLE-2017-BLG-0364.

For the 2L1S parameters, as expected, ρ and q are slightly larger than our heuristic analysis for the Wide A model because of the offset between the source trajectory from the center of the caustic, while the other three von Schlieffen–type models significantly deviate from our estimate. The PSPL parameters and the source flux of the Wide A model are consistent with those obtained by excluding the anomaly, but the other three models do not exhibit such consistency. Figure 1 also shows the cumulative $\Delta\chi^2$ relative to the Wide A model of the four models, in which the other three models are disfavored not only inside the anomalous region. For most microlensing planetary events, the planetary signal itself is less significant than the microlensing signal (i.e., the host-star signal), so degenerate planetary models have little influence on the PSPL parameters of the host star. However, for the present case, the maximum magnification due to the host star ($\Delta A \sim 0.3$) is only half of the maximum magnification due to the planet, so the fitting to the planetary signal affects the fitting to the host star and results in χ^2 differences outside the anomalous region.

Compared to the Wide A model, the Wide B, Wide C, and Wide D models are disfavored by $\Delta\chi^2 = 27$, 32, and 63, respectively. We also try high-order effects but the three models are still disfavored by $\Delta\chi^2 > 20$, so we exclude them.

For the close topology ($s < 1$), the grid search finds two models. As shown in Figure 3, the source crosses the binary axis either inside or outside the planetary caustics relative to the central caustic, so we label them as the "Close Inner" and "Close Outer" models, and their parameters are given in Table 2. We also try the 1L2S modeling, and the resulting parameters are shown in Table 2. The two close models and the 1L2S model are disfavored by $\Delta\chi^2 > 210$ compared to the Wide A model. Figure 4 displays a close-up of the anomaly together with the three models, and the three models cannot fit the anomaly. Hence, we exclude them and only further investigate the Wide A model. The planet–host mass ratio, $q \sim 10^{-4}$, and the scaled planet–host separation, $s \sim 1.8$, indicate a low mass-ratio planet in a wide orbit.

In addition, the inclusion of higher-order effects yields a constraint on $\pi_{\rm E,\parallel} = -0.05 \pm 0.15$, where $\pi_{\rm E,\parallel} \sim \pi_{\rm E,E}$ is the minor axes of the elliptical parallax contour and is approximately parallel with the direction of Earth's acceleration. For the major axes of the parallax contour, $\pi_{\rm E,\perp} \sim \pi_{\rm E,N}$, there is no useful constraint because of $\sigma(\pi_{\rm E,\perp}) \sim 1$ while the typical value of $\pi_{\rm E,\perp}$ is ∼0.1. We will adopt $\pi_{\rm E,\parallel}$ in the Bayesian analysis of Section 4 to estimate the lens' physical parameters.

3.3. KMT-2017-BLG-1057

Figure 5 shows a ∼1.5 day dip 5 days after the peak of the PSPL model, followed by a half-day bump. Such an anomaly is likely due to a minor-image perturbation and is similar to the anomaly of KMT-2017-BLG-1194 (Zang et al. 2023). A grid search yields only one local minimum whose $\Delta\chi^2 < 50$ than other local minima, and further numerical analysis, including the hotter MCMC process cannot find any degenerate models. Figure 6 exhibits the caustic geometry and Table 3 presents the 2L1S parameters. The source first passes on the relatively demagnified regions between the two minor-image planetary caustics and then crosses one of the caustics, but due to the poor coverage during the caustic crossing, finite-source effects

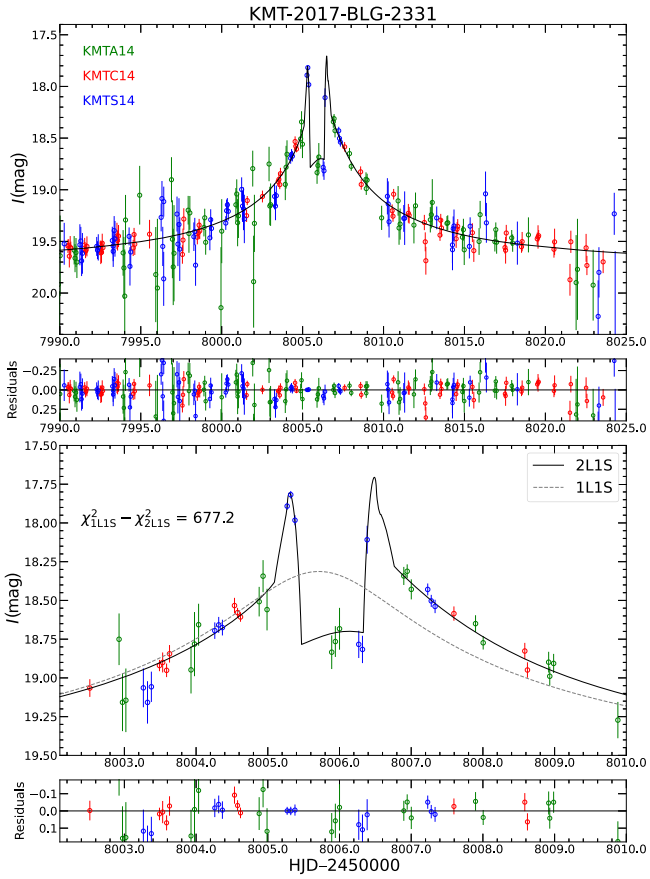

Figure 10. Observed data and the 2L1S model for KMT-2017-BLG-2331.

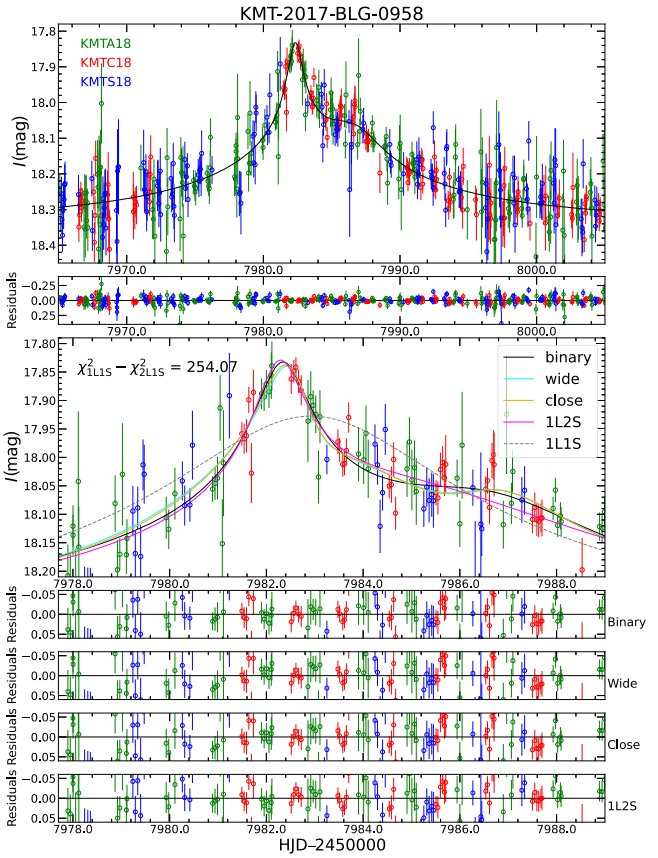

Figure 11. Observed data together with three 2L1S models and the 1L2S model for KMT-2017-BLG-0958. All models can fit the data well and thus this is only a candidate planetary event.

are not measured and a point-source model is consistent within the 1σ level to the best-fit model. Nevertheless, we obtain a tight constraint on the upper limit of ρ, with $\rho < 0.0025$ at 3σ, which will be used in the estimate of the lens properties.

Due to the short $t_{\rm E}$ and faint event, the inclusion of higher-order effects only improves the fitting by $\Delta\chi^2 < 1$ and $\sigma(\boldsymbol{\pi}_{\rm E,\parallel}) > 0.4$, which are not useful for the Bayesian analysis. The mass ratio, $q = 1.15^{+0.27}_{-0.18} \times 10^{-4}$, indicates a new low-$q$ planet.

3.4. OGLE-2017-BLG-0364

The anomaly of OGLE-2017-BLG-0364, is a bump centered on $t_{\rm anom} \sim 7846.5$, as shown in Figure 7. A PLPS fit by excluding the anomaly yields $(t_0, u_0, t_{\rm E}) = (7831.3, 0.05, 18)$. Using Equations (6), (7), and (8), we estimate

$$|\alpha| = 0.06 \text{ rad}, \quad s_+ \sim 1.51, \quad s_- \sim 0.66. \tag{13}$$

Due to the faint source, it is of low probability that the source is large enough to fully envelop the caustic, and the anomaly is not well covered, so we cannot estimate ρ and q from a heuristic analysis.

A grid search identifies three local minima whose $\Delta\chi^2 < 100$ than other local minima, including two close models (i.e., Close Inner and Close Outer) and one wide model. A hotter MCMC analysis, as shown in Figure 8, further finds three wide models, and we label them as Wide A, Wide B, and Wide C. Their model curves are shown in Figure 7, their caustic geometries are exhibited in Figure 9, and the resulting parameters from the MCMC and downhill approaches are presented in Table 4. The resulting α and s are basically consistent with the estimate above. The Wide A and Wide B models are nearly symmetric, i.e., a source interacting with a ridge before and after crossing the quadrilateral caustic, respectively, so there are three peaks over the anomaly. The Wide C model passes through by the center of the caustic, with a source that is roughly the same size as the caustic, so there is only one nearly symmetric peak. For all of the models, finite-source effects are measured.

Following our criterion of a degenerate model, we exclude the Close Outer model because of $\Delta\chi^2 = 27.2$ compared to the best-fit model, Wide A, while the Wide B, Wide C, and Close Inner models are only disfavored by $\Delta\chi^2 = 14.9$, 20, and 18.9, respectively. We also check the 1L2S model, and Table 4 lists the 1L2S parameters. We find $\Delta\chi^2 = 32.7$ and that the 1L2S model cannot well fit the OGLE and KMTC data of the anomaly. Hence, we rule out the 1L2S possibility. For the high-order effects, there is no useful constraint, with $\sigma(\boldsymbol{\pi}_{\rm E,\parallel}) > 0.3$, due to the short and faint event.

3.5. KMT-2017-BLG-2331

As shown in Figure 10, the peak of KMT-2017-BLG-2331 exhibits a double-horned profile connected by a trough, which is similar to the light curves produced by a resonant caustic (e.g., Yee et al. 2014; Udalski et al. 2018) or a central caustic (e.g., Udalski et al. 2005; Dong et al. 2009). The grid search finds only one local minimum whose $\Delta\chi^2 < 100$ than other local minima and further investigation including hotter MCMC does not locate any degenerate models. Figure 6 displays the

Table 5
Lensing Parameters for KMT-2017-BLG-0958

Parameters	2L1S			1L2S
	Binary	Planet Wide	Planet Close	
χ^2/dof	2570.03/2570	2575.63/2570	2575.53/2570	2584.69/2570
$t_{0,1}$ (HJD′)	$7983.58^{+0.09}_{-0.08}$	$7983.30^{+0.07}_{-0.07}$	$7983.56^{+0.07}_{-0.08}$	$7984.81^{+0.39}_{-0.31}$
$t_{0,2}$ (HJD′)				$7982.29^{+0.04}_{-0.04}$
$u_{0,1}$	$0.030^{+0.008}_{-0.006}$	$0.023^{+0.007}_{-0.004}$	$0.008^{+0.002}_{-0.002}$	$0.074^{+0.023}_{-0.021}$
$u_{0,2}$				$-0.009^{+0.002}_{-0.003}$
t_E (days)	$97.10^{+19.90}_{-15.47}$	$134.59^{+32.66}_{-29.11}$	$291.83^{+70.11}_{-56.05}$	$59.58^{+20.02}_{-12.46}$
ρ_1 (10^{-3})	<11	<8	<4	
ρ_2 (10^{-3})				<30
$q_{f,I}$				$0.17^{+0.05}_{-0.04}$
α (rad)	$-0.44^{+0.04}_{-0.05}$	$1.94^{+0.02}_{-0.02}$	$1.94^{+0.03}_{-0.02}$	
s	$0.20^{+0.03}_{-0.02}$	$1.50^{+0.04}_{-0.04}$	$0.65^{+0.02}_{-0.02}$	
$q(10^{-3})$	$0.96^{+1.29}_{-0.47} \times 10^3$	$6.19^{+1.89}_{-1.24}$	$2.89^{+0.67}_{-0.60}$	
$\log q$	$-0.020^{+0.371}_{-0.294}$	$-2.209^{+0.116}_{-0.097}$	$-2.540^{+0.091}_{-0.100}$	
$f_{S,KMTC}$	$0.009^{+0.002}_{-0.002}$	$0.006^{+0.002}_{-0.001}$	$0.003^{+0.001}_{-0.001}$	$0.018^{+0.006}_{-0.005}$
$f_{B,KMTC}$	$0.711^{+0.001}_{-0.002}$	$0.715^{+0.001}_{-0.001}$	$0.716^{+0.001}_{-0.001}$	$0.705^{+0.004}_{-0.005}$

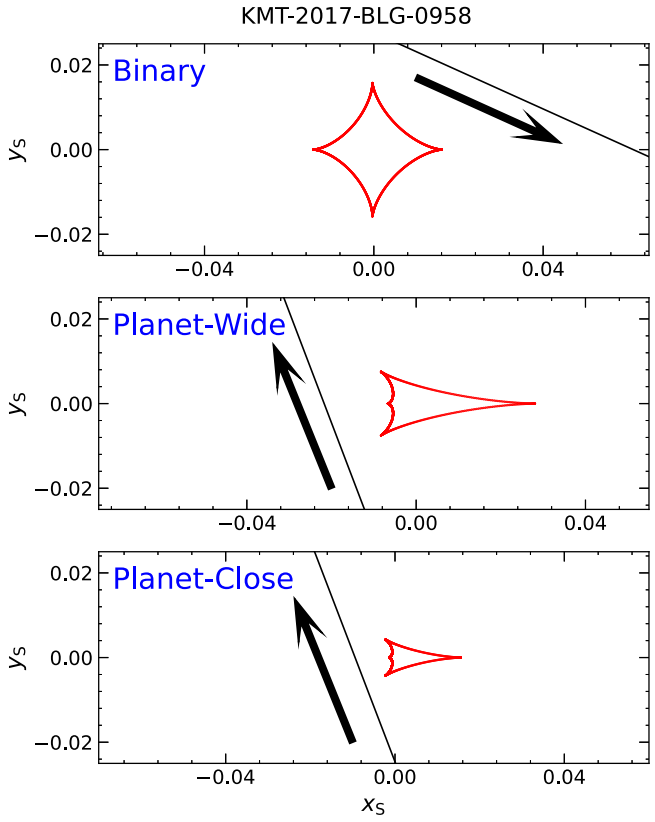

Figure 12. Caustic geometries of the candidate planetary event, KMT-2017-BLG-0958.

caustic geometry for the best-fit model. As expected, the source crosses a resonant caustic. The two sharp peaks are due to the caustic crossings of two sides of the caustic, and the trough is caused by the relatively demagnified regions between them.

Parameters from the MCMC are presented in Table 3. Although there are several large gaps in the coverage of the anomaly, finite-source effects are measured, with $\rho = 2.04^{+0.32}_{-0.26} \times 10^{-3}$. This is a new Jovian mass-ratio planet. Due to the faintness of the event, we do not get a useful constraint on π_E.

3.6. KMT-2017-BLG-0958

The anomaly of KMT-2017-BLG-0958 is a two-bump feature, centered on $t = 7982$ and $t = 7987$, respectively, as shown in Figure 11. Both a 2L1S and a 1L2S model can produce such an anomaly. For the 2L1S modeling, we find three degenerate models. The first model has a stellar-binary mass ratio and provides the best fit to the observed data. The other two models have a super-Jovian mass ratio and are disfavored by $\Delta\chi^2 = 6$, and we label them as "Planet Close" ($s < 1$) and "Planet Wide" ($s > 1$). Figure 12 displays the caustic geometries, and Table 5 presents the lensing parameters. Due to the faintness of the event, neither of the models has a good constraint on t_E. Finite-source effects are not measured for any models.

We also check the 1L2S model and find it disfavored by only $\Delta\chi^2 = 15$ to the best-fit 2L1S model, and even when we impose $\rho_2 = 0$ the 1L2S model is still disfavored by only $\Delta\chi^2 = 16$, so we cannot rule out the 1L2S model by a kinematic argument that the resulting μ_{rel} is unlikely. Due to the severe extinction for this event, with $A_K = 0.87$ (Gonzalez et al. 2012), the V-band data have no microlensing signal and we cannot exclude the 1L2S model by a color argument for different source colors (Gaudi 1998).

In summary, we conclude that the lens–source system could be either 2L1S or 1L2S and if the latter a stellar-binary interpretation is preferred. Because this is a candidate planetary event, we do not conduct further analysis.

4. Lens Properties

4.1. Preamble

We estimate the lens properties in this section. As in Section 3.1, we first introduce the common processes. From Equations (1) and (3), the lens mass, M_L, and the lens distance, D_L, are related to the angular Einstein radius and the microlensing parallax by Gould (1992, 2000)

$$M_L = \frac{\theta_E}{\kappa \pi_E}, \qquad D_L = \frac{\mathrm{au}}{\pi_E \theta_E + \pi_S}, \tag{14}$$

where π_S is the source parallax.

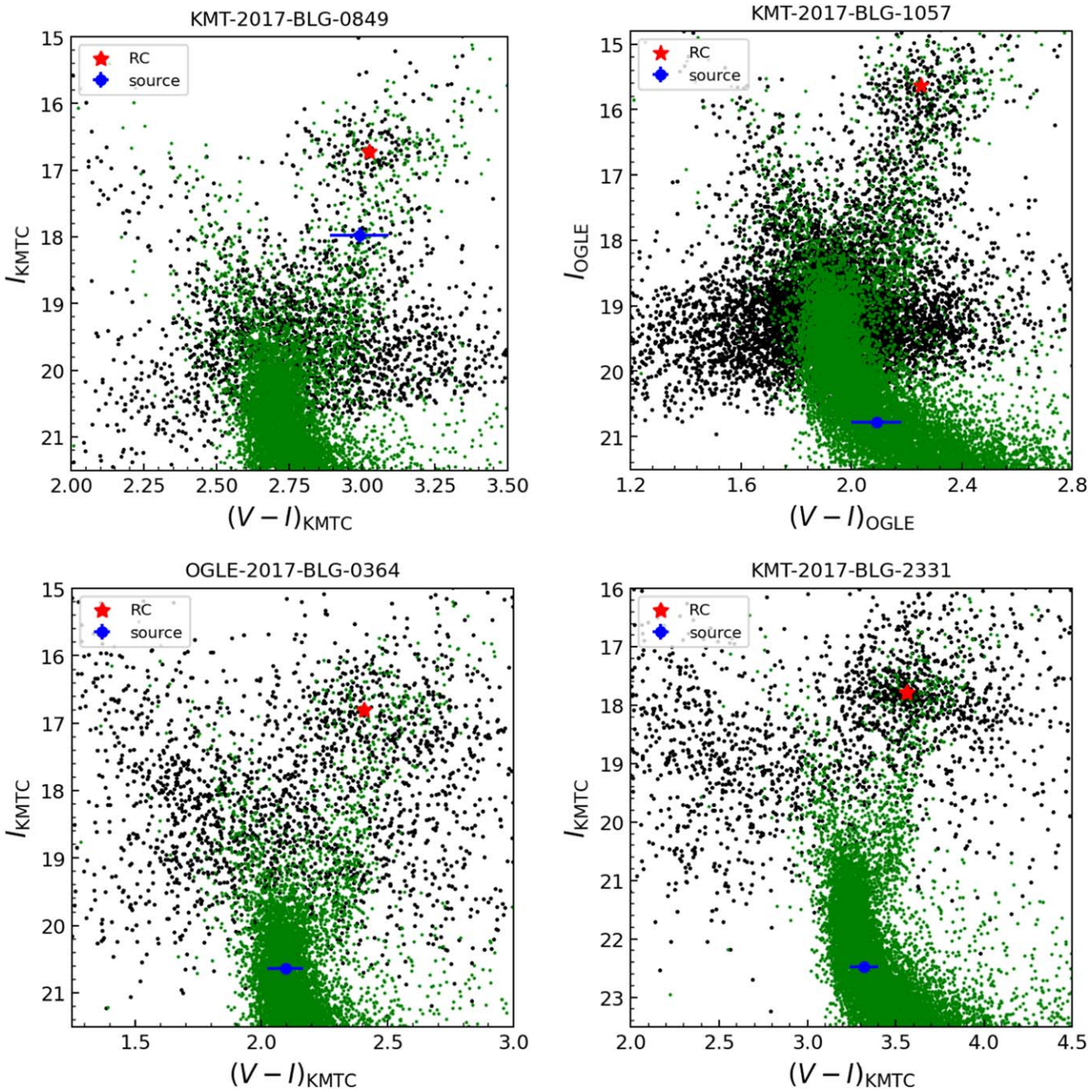

Figure 13. CMD for the four unambiguous planetary events. The CMDs of KMT-2017-BLG-0849, KMT-2017-BLG-1057, and KMT-2017-BLG-2331 are constructed using the KMTC field stars, and the CMD of OGLE-2017-BLG-0364 is built using the OGLE-III star catalog (Szymański et al. 2011). For each panel, the red asterisk and the blue dot represent the centroid of the red-giant clump and the source star, respectively. The green dots represent the HST CMD of Holtzman et al. (1998), whose centroid of the red-giant clump $(V-I, I)_{\rm cl,HST} = (1.62, 15.15)$ (Bennett et al. 2008) is matched to that of KMTC or OGLE-III.

The angular Einstein radius can be derived through $\theta_{\rm E} = \theta_*/\rho$. To estimate θ_*, we locate the source on a color–magnitude diagram (CMD; Yoo et al. 2004), which is constructed from the ambient stars around the event. From the CMD, we estimate the centroid of the red-giant clump as $(V-I,\ I)_{\rm cl}$, for which the dereddened color and magnitude, $(V-I, I)_{\rm cl,0}$, are adopted from Bensby et al. (2013) and Table 1 of Nataf et al. (2013), respectively. The source apparent magnitude is from the light-curve analysis. For the source color, which is independent of the 2L1S model, neither event has a sufficient V-band signal-to-noise ratio to determine the source color by a regression of the KMTC V versus I flux. Therefore, we calibrate the Hubble Space Telescope (HST) CMD of Holtzman et al. (1998) to the KMTC CMD using $I_{\rm cl}$ of red-giant clumps and then estimate the source color by the color of HST field stars within the 5σ brightness of the source star. Using the color–surface brightness relations of Adams et al. (2018), we obtain the angular source radius θ_*. Then, we derive $\theta_{\rm E}$ by θ_*/ρ and $\mu_{\rm rel}$ by $\theta_{\rm E}/t_{\rm E}$.

Figure 13 displays CMDs of the four planetary events. Table 6 summarizes the CMD parameters, and the resulting θ_*, $\theta_{\rm E}$, and $\mu_{\rm rel}$.

For the microlensing parallax, only KMT-2017-BLG-0849 has a useful constraint on $\pi_{\rm E}$. Therefore, we estimate the

Table 6
CMD Parameters, θ_*, θ_E, and μ_{rel} for the Four Planetary Events

Parameter	KB170849	KB171057	OB170364				KB172331
			Wide A	Wide B	Wide C	Close Inner	
$(V-I)_{cl}$	N.A.	N.A.	N.A.	⟵	⟵	⟵	N.A.
I_{cl}	16.72 ± 0.04	15.63 ± 0.03	16.81 ± 0.09	⟵	⟵	⟵	17.78 ± 0.03
$I_{cl,0}$	14.30 ± 0.04	14.30 ± 0.04	14.62 ± 0.04	⟵	⟵	⟵	14.52 ± 0.04
$(V-I)_S$	N.A.	N.A.	N.A.	⟵	⟵	⟵	N.A.
I_S	17.98 ± 0.12	20.90 ± 0.08	20.64 ± 0.03	20.47 ± 0.05	20.43 ± 0.05	20.69 ± 0.02	22.48 ± 0.08
$(V-I)_{S,0}$	1.03 ± 0.10	0.92 ± 0.09	0.75 ± 0.07	0.75 ± 0.07	0.74 ± 0.07	0.75 ± 0.07	0.82 ± 0.08
$I_{S,0}$	15.55 ± 0.13	19.57 ± 0.09	18.45 ± 0.10	18.28 ± 0.11	18.24 ± 0.11	18.50 ± 0.10	19.22 ± 0.09
θ_* (μas)	3.59 ± 0.81	0.473 ± 0.045	0.681 ± 0.055	0.739 ± 0.062	0.746 ± 0.063	0.668 ± 0.054	0.509 ± 0.043
θ_E (mas)	0.201 ± 0.047	>0.19	0.341 ± 0.058	0.238 ± 0.065	0.067 ± 0.017	0.607 ± 0.173	0.246 ± 0.041
μ_{rel} (mas yr^{-1})	2.80 ± 0.65	>2.0	6.70 ± 1.15	5.43 ± 1.50	1.57 ± 0.40	11.49 ± 3.28	1.86 ± 0.34

Note. $(V-I)_{cl,0} = 1.06 \pm 0.03$ (Bensby et al. 2013). Event names are abbreviations, e.g., KMT-2017-BLG-0849 is shortened to KB170849. The upper limits on θ_E and μ_{rel} are 3σ.

Table 7
Lensing Physical Parameters for the Four Planetary Events from a Bayesian Analysis

Event	Model	Physical Properties					Relative Weight Gal. Mod.
		($M_\odot$)	($M_\oplus$)	(kpc)	(au)	(mas yr^{-1})	
KB170849		$0.19^{+0.23}_{-0.09}$	$6.39^{+7.80}_{-3.09}$	$7.22^{+0.82}_{-0.99}$	$2.73^{+0.68}_{-0.62}$	$3.14^{+0.65}_{-0.62}$	
KB171057		$0.57^{+0.37}_{-0.29}$	$23.5^{+15.0}_{-12.0}$	$6.50^{+0.81}_{-1.62}$	$2.36^{+0.69}_{-0.62}$	$4.55^{+1.58}_{-1.14}$	
OB170364	Wide A	$0.49^{+0.35}_{-0.28}$	$75.8^{+54.5}_{-42.9}$	$7.86^{+1.08}_{-1.99}$	$3.79^{+0.76}_{-0.89}$	$6.53^{+1.14}_{-0.94}$	0.60
	Wide B	$0.35^{+0.33}_{-0.20}$	$60.9^{+57.9}_{-35.4}$	$8.38^{+0.92}_{-1.66}$	$3.00^{+0.80}_{-0.69}$	$5.41^{+1.41}_{-1.05}$	1.00
	Wide C	$0.10^{+0.16}_{-0.05}$	$20.4^{+33.8}_{-10.7}$	$8.98^{+0.80}_{-0.88}$	$1.27^{+0.49}_{-0.30}$	$2.11^{+0.84}_{-0.51}$	0.18
	Close Inner	$0.55^{+0.38}_{-0.30}$	256^{+176}_{-139}	$6.84^{+1.54}_{-1.86}$	$1.96^{+0.43}_{-0.51}$	$8.18^{+1.63}_{-1.37}$	0.11
KB172331		$0.40^{+0.32}_{-0.21}$	171^{+137}_{-88}	$8.03^{+0.84}_{-1.05}$	$2.14^{+0.48}_{-0.42}$	$2.06^{+0.43}_{-0.34}$	

physical parameters of the planetary systems from a Bayesian analysis using a Galactic model as priors. The Galactic model and the basic procedures are the same as used by Yang et al. (2021), assuming that the planetary occurrence rate is independent of the host-star properties (e.g., host mass). We refer the reader to that work for details. The only additional procedure in our Bayesian analysis is that we exclude trial events for which the lens flux exceeds the upper limits of the lens flux, $I_{L,limit}$, obtained from the light-curve and imaging analysis. We adopt the mass–luminosity relation of Wang et al. (2018).

Table 7 and Figure 14 show the posterior distributions from the Bayesian analysis, including the host mass, M_{host}, the planetary mass, M_{planet}, the lens distance, D_L, the projected planet–host separation, $r_\perp$, and the heliocentric lens–source relative proper motion, $\mu_{hel,rel}$. For OGLE-2017-BLG-0364, we also provide the relative probability from the Galactic model for each degenerate model.

4.2. KMT-2017-BLG-0849

We use stars in the $2' \times 2'$ square centered on the event to construct the CMD. The source is probably a red giant and the color, $(V-I)_{S,0} = 1.03 \pm 0.10$, is derived by matching the HST CMD to the KMTC CMD. We adopt the 3σ upper limit of the blended light as the upper limits of the lens flux, i.e., $I_{L,limit,KMTC} = 18.7$. The low relative proper motion, $\mu_{rel} = 2.80 \pm 0.65$ mas yr^{-1}, indicates a bulge lensing system.

The host star from the Bayesian analysis prefers a low-mass M dwarf. The planet is likely a super-Earth/mini-Neptune. The preferred projected planet–host separation, $r_\perp \sim 2$ au, favors that this planet is located well beyond the snow line of the planetary system (Kennedy & Kenyon 2008).

4.3. KMT-2017-BLG-1057

The CMD is constructed from the OGLE-III field stars (Szymański et al. 2011) within $2.5'$ centered on the event, and we calibrate the KMTC flux to the OGLE flux by matching bright field stars. The source is probably a G dwarf. The 3σ upper limit of the blended light is $I_{B,KMTC} = 20.62$. Considering the mottled background (Park et al. 2004) of the crowded stellar field, we adopt $I_{L,limit,KMTC} = 20.0$. With the constraint on ρ from the light-curve analysis, we obtain $\theta_E > 0.19$ mas and $\mu_{rel} > 2.0$ mas yr^{-1} at 3σ. The likelihood distribution of θ_E used for the Bayesian analysis is derived by the minimum χ^2 for the lower envelope of the (χ^2 versus ρ) diagram and the θ_* distribution.

According to the Bayesian analysis, the host prefers a K or M dwarf, and the planetary mass prefers a super-Neptune mass. The lensing system can be located in either the bulge or the disk.

4.4. OGLE-2017-BLG-0364

We build the CMD using the KMTC stars within a $4' \times 4'$ square centered on the event. The source color is also estimated by the HST CMD and slightly varies among different models because of the different source brightnesses. The blended flux

Table 8
Information of the Unambiguous Planetary Events from the KMTNet 2017 Subprime Fields

Event Name	KMTNet Name	$\log q$	s	Method	$\Delta\chi^2$	Reference
KB171194	KB171194	-4.582 ± 0.058	0.806 ± 0.010	Discovery		Zang et al. (2023)
KB171003	KB171003	-4.373 ± 0.144	0.910 ± 0.005	Discovery	0.0	Zang et al. (2023)
		-4.260 ± 0.152	0.889 ± 0.004		0.2	
OB171806	KB171021	-4.352 ± 0.171	0.857 ± 0.008	Discovery	0.0	Zang et al. (2023)
		-4.392 ± 0.180	0.861 ± 0.007		0.2	
		-4.441 ± 0.168	1.181 ± 0.011		8.3	
		-4.317 ± 0.126	1.190 ± 0.012		8.4	
OB171691	KB170752	-4.013 ± 0.152	1.003 ± 0.014	Recovery	0.0	Han et al. (2022)
		-4.150 ± 0.141	1.058 ± 0.011		0.4	
KB170849	KB170849	-3.998 ± 0.053	1.804 ± 0.049	Discovery		This work
KB171057	KB171057	-3.925 ± 0.101	0.919 ± 0.005	Discovery		This work
OB170364	KB171396	-3.341 ± 0.079	1.504 ± 0.016	Recovery		This work
KB172331	KB172331	-2.891 ± 0.044	1.027 ± 0.020	Recovery		This work
KB171146	KB171146	-2.699 ± 0.076	0.734 ± 0.014	Recovery	0.0	Shin et al. (2019a)
		-2.347 ± 0.092	1.148 ± 0.014		9.5	
KB172509	KB172509	-2.360 ± 0.053	0.925 ± 0.007	Recovery		Han et al. (2021)
KB171038	KB171038	-2.276 ± 0.025	0.851 ± 0.003	Recovery		Shin et al. (2019a)
OB171099	KB172336	-2.192 ± 0.053	1.137 ± 0.014	Recovery		Han et al. (2021)
OB171140	KB171018	-2.142 ± 0.039	0.871 ± 0.013	Recovery	0.0	Calchi Novati et al. (2018)
		-2.137 ± 0.045	0.870 ± 0.014		1.0	
OB171630	KB171237	-2.114 ± 0.009	1.84 ± 0.02	Recovery	0.0	in preparation
		-2.119 ± 0.008	0.54 ± 0.01		0.4	
KB172197	KB172197	-1.721 ± 0.060	0.723 ± 0.008	Recovery	0.0	Han et al. in preparation
		-1.721 ± 0.060	1.499 ± 0.028		0.1	

Note. For each planet, we only consider the models that have $\Delta\chi^2 < 10$ compared to the best-fit model. "Discovery" represents that the planet was discovered using AnomalyFinder, and "Recovery" means that the planet was first discovered from by-eye searches and then recovered by AnomalyFinder.

is consistent with zero and we adopt $I_{\rm L,limit,KMTC} = 20.0$ for considering the mottled background.

Because of $\ell = -5.3617$, $D_{\rm S} = 10.0^{+0.9}_{-0.8}$ kpc according to the Bayesian analysis, and thus the resulting lens distances are farther than most microlensing events. The Wide A and Wide B models are favored. The Wide C and Close Inner models are disfavored because of the small $\theta_{\rm E}$ and the high $\mu_{\rm rel}$, respectively. The Wide A and Wide B models have almost the same preferred lensing properties, i.e., a sub-Saturn orbiting an M dwarf at a projected separation of $\sim$3 au. The nature of the lens could be resolved by future high-resolution imaging because the Wide C and Close Inner models have different $\mu_{\rm rel}$ than the Wide A and Wide B models. This can certainly be done at first light of the Extremely Large Telescope (ELTs; roughly 2030) when the separation will be about 80 mas (5 times the imaging FWHM for the European ELT K band). And it may be possible with Keck as early as 2027, provided that the Wide A and Wide B models are correct and the host is sufficiently bright.

4.5. KMT-2017-BLG-2331

The CMD size for KMT-2017-BLG-2331 is a $4' \times 4'$ square centered on the event. Because of the high extinction $A_I \sim 3.8$ and the low stellar surface density, the mottled background is negligible (fluctuations > 21 mag). We use the 3σ upper limit of the blended light, $I_{\rm B,KMTC} = 19.8$, as $I_{\rm L,limit,KMTC}$.

The Bayesian analysis prefers a sub-Jupiter-mass planet orbiting an M dwarf. The lensing system is probably located in the Galactic bulge, consistent with the low proper motion, $\mu_{\rm rel} \sim 2$ mas yr^{-1}.

5. Discussion: A Complete Sample from the First 4 yr KMTNet Survey

In this paper, we have presented an analysis of four new planets. Together with nine that are already published and three that will be published elsewhere, there are 16 clear planets from the 2017 KMTNet subprime data. Among these, the anomaly of OGLE-2017-BLG-0668/KMT-2017-BLG-1145 was generated primarily by two sources. The current AnomalyFinder algorithm cannot yield a complete sample for such events (Kuang et al. 2022), so we exclude this event from the AnomalyFinder planetary sample of the 2017 subprime fields. Table 8 summarizes the 15 planets, including $\log q$, s, discovery method, and $\Delta\chi^2$ compared to the best-fit models for degeneracy. Among them, five were discovered by AnomalyFinder and 10 were first discovered using by-eye searches and then recovered by AnomalyFinder. A striking feature of this sample is that all AnomalyFinder-discovery

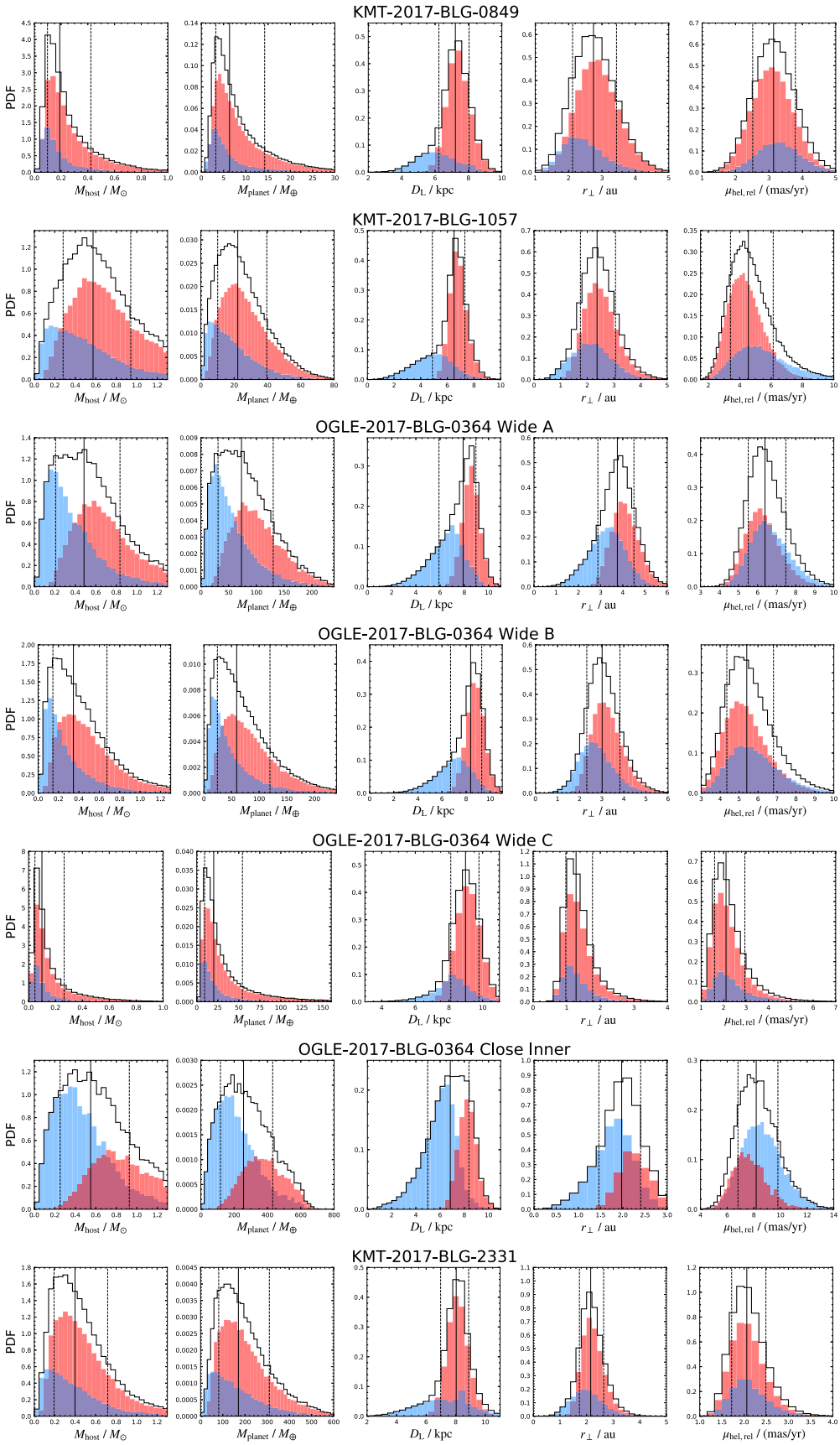

Figure 14. Bayesian posterior distributions (PDF) of the mass of the host star, $M_{\rm host}$, the planetary mass, $M_{\rm planet}$, the lens distance, $D_{\rm L}$, the projected planet–host separation, $r_\perp$, and the lens–source relative proper motion in the heliocentric frame, $\mu_{\rm hel,rel}$. In each panel, the solid black line and the two dashed black lines represent the median value and the 15.9% and 84.1% percentiles of the distribution. The solid black histogram shows the total distribution, and the bulge and disk lens distributions are shown in red and blue, respectively.

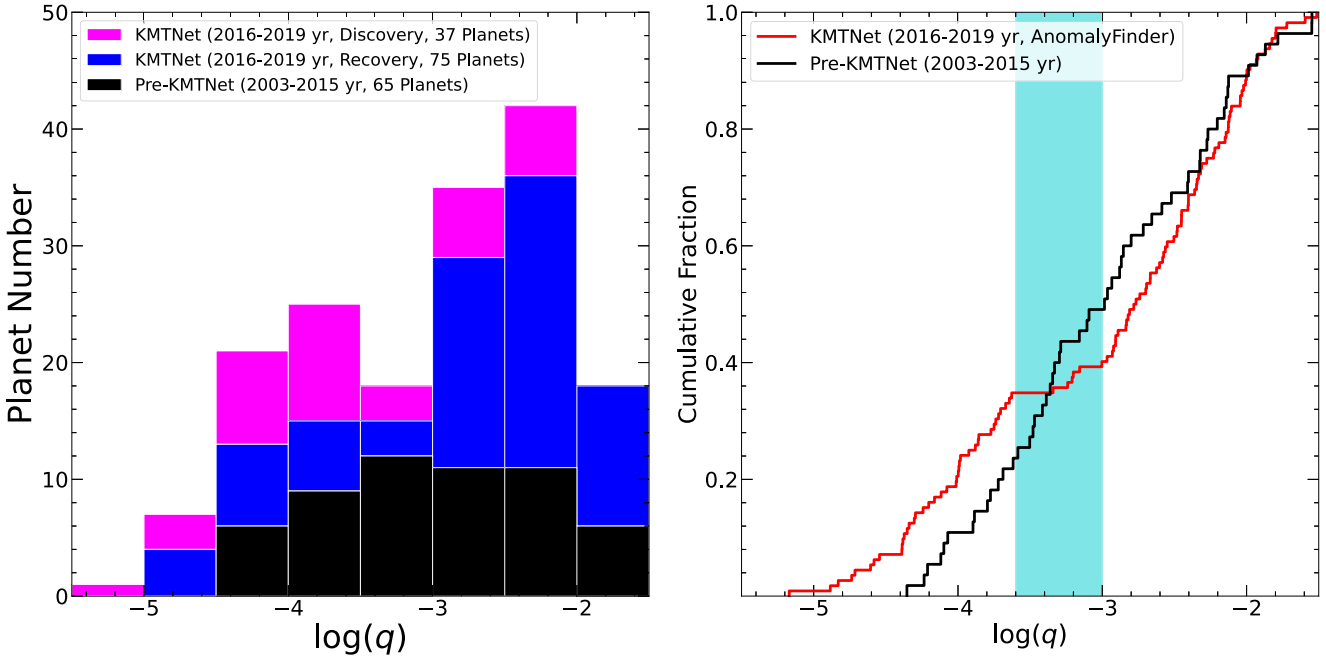

Figure 15. Left: histogram distributions of $\log q$ for the 2016–2019 KMTNet AnomalyFinder-discovery (magenta) and AnomalyFinder-recovery (blue) planets, and the planets detected before KMTNet's regular survey (black). Right: cumulative distributions of $\log q$ for the pre-KMTNet planets and the 2016–2019 KMTNet AnomalyFinder planets, which are the sum of the AnomalyFinder-discovery and AnomalyFinder-recovery planets shown in the left panel. The dark turquoise region indicates the "sub-Saturn desert" ($\log q = [-3.6, -3.0]$) in the KMTNet sample.

planets have $\log q < -3.0$, and these comprise 5/7 of the $\log q < -3.0$ planets, demonstrating AnomalyFinder's important role in the detection of low-q planets, while by-eye searches mainly detected massive planets.

With the complete planetary sample of the 2017 subprime field, we have completed the planetary sample from the first 4 yr of KMTNet data (2016–2019). Below we briefly review this sample, to understand the impact of KMTNet and AnomalyFinder. We follow the criteria of Zang et al. (2024) for the definition of a planetary event. That is, we exclude planets in binary-star systems, planets with degenerate stellar-binary models ($\log q > -1.5$ with $\Delta\chi^2 < 10$), and planets with the 2L1S/1L2S degeneracy (a 1L2S model with $\Delta\chi^2 < 16$). The difference is that we keep planets with large uncertainties in $\log q$ because we do not attempt to study the mass-ratio function here.

In total, we form a sample of 112 planets, with 28 planets per year on average. The seasonal distributions (23, 30, 35, and 24) for 2016–2019, respectively, are consistent with Poisson variations. Of them, 37 were AnomalyFinder-discovery planets, so AnomalyFinder increases the KMTNet planetary detections by 50%. In 2015, KMTNet conducted commissioning observations toward four fields with a cadence of $\Gamma = 6$ hr^{-1}. Since 2016, KMTNet has devoted about half of its time to subprime fields, and 52 (i.e., 46%) planets are from subprime fields. Below we mainly focus on a discussion of the distribution of q, because the distributions of the other parameters (e.g., caustic crossing and anomaly type) have been investigated by Jung et al. (2023) and Zang et al. (2023) in detail using the subgroups of this sample and we do not find a big difference.

We adopt the best-fit model of each planet, and the left panel of Figure 15 shows the mass-ratio distributions for the AnomalyFinder-discovery and AnomalyFinder-recovery planets, respectively. Similar to the 2017 subprime sample, most (25) AnomalyFinder-discovery planets have $\log q < -3$, increasing the number of KMTNet $\log q < -3$ planets by 125%. The fundamental reason is that for most cases AnomalyFinder can find significantly more subtle signals than by-eye searches, as previously found by Zang et al. (2022b) and Hwang et al. (2022) for smaller samples. For massive planets ($\log q > -3$), by-eye searches are basically sufficient and AnomalyFinder increases the number by only 22%.

Using the same criteria above that are listed, we form a microlensing planetary sample from 2003 (i.e., the year of the first microlensing planet) to 2015 (i.e., the year before KMTNet's regular survey). The only difference is that we keep three planets in binary-star systems (Gould et al. 2014; Poleski et al. 2014; Bennett et al. 2016). We exclude the planet OGLE-2015-BLG-1771Lb, for which the planetary signal was detected by the commissioning data of KMTNet. For the other two cases with the KMTNet data, OGLE-2015-BLG-0954Lb (Shin et al. 2016; Bennett et al. 2017) and OGLE-2015-BLG-1670Lb (Ranc et al. 2019), the planetary signal can be well covered by the OGLE and Microlensing Observations in Astrophysics (MOA) data. In total, this sample contains 65 planets, and the mass-ratio distribution is also shown in the left panel of Figure 15. Overall, the first 4 yr KMTNet microlensing survey nearly tripled the microlensing planetary sample. The most significant advance occurs at the low end of the mass-ratio distribution. The KMTNet sample reaches mass ratios about an order of magnitude lower than the pre-KMTNet sample and expands the $\log q < -4$ sample 5 times. Furthermore, the pre-KMTNet sample consists of planets from several groups and the resulting statistical samples have relatively small sizes, with six planets in the sample from the Microlensing Follow Up Network (Gould et al. 2010), three planets in the sample from the Probing Lensing Anomalies NETwork follow-up network (Cassan et al. 2012), 22 planets in the sample from the MOA group (Suzuki et al. 2016), and eight planets in the sample from a combination of 4 yr of

OGLE + MOA + Wide-field Infrared Survey Explorer data (Shvartzvald et al. 2016). Combined with planets after 2020, KMTNet will form a statistical sample an order of magnitude larger than any previous samples.

The right panel of Figure 15 displays the cumulative mass-ratio distribution for the KMTNet and pre-KMTNet samples. Besides the low-q planets, another striking difference between the two samples is that the KMTNet sample shows a plateau between $\log q = [-3.6, -3.0]$, while the pre-KMTNet sample does not.[20] This mass-ratio desert is consistent with the prediction from the standard core accretion runaway growth scenario (Ida & Lin 2004; Mordasini et al. 2009). We refer to this desert as the sub-Saturn desert, considering that the typical hosts are expected to be M and K dwarfs for microlensing planets.

The sub-Saturn desert in the KMTNet sample was first noticed by Yang et al. (2020) mostly using a sample of 2016 and 2017 KMTNet planets from by-eye searches. However, because the sample of Yang et al. (2020) was incomplete and not homogeneously selected and the pre-KMTNet sample does not show such a desert, Yang et al. (2020) concluded that the discrepancy between the two samples was most likely caused by publication bias. However, the complete and homogeneously selected sample of 2018 and 2019 KMTNet planets, together corrected by the KMTNet and AnomalyFinder detection efficiency, strongly supports the existence of the sub-Saturn desert in the KMTNet sample (Zang et al. 2024). And now, the complete sample of 2016 and 2017 KMTNet planets confirms the sub-Saturn desert. A more detailed study of the sub-Saturn desert will be presented together with the 2021 AnomalyFinder planetary sample (I.-G. Shin et al. 2024, in preparation).

Acknowledgments

We appreciate the anonymous referee for helping to improve the paper. Y.G., W.Za., R.Z., H.Y., S.M., J.Z., R.K., Q.Q., and W.Zh. acknowledge support by the National Natural Science Foundation of China (grant No. 12133005). W.Za. acknowledges the support from the Harvard-Smithsonian Center for Astrophysics through a CfA Fellowship. This research has made use of the KMTNet system operated by the Korea Astronomy and Space Science Institute (KASI) at three host sites of CTIO in Chile, SAAO in South Africa, and SSO in Australia. Data transfer from the host site to KASI was supported by the Korea Research Environment Open NETwork (KREONET). This research was supported by KASI under the R&D program (project No. 2024-1-832-01) supervised by the Ministry of Science and ICT. The work by R.P. and J.S. was supported by Polish National Agency for Academic Exchange grant "Polish Returns 2019." J.C.Y. and I.-G.S. acknowledge support from N.S.F grant No. AST-2108414. The work by C.H. was supported by the grants of National Research Foundation of Korea (2019R1A2C2085965 and 2020R1A4A2002885). Y.S. acknowledges support from BSF grant No. 2020740. The authors acknowledge the Tsinghua Astrophysics High-Performance Computing platform at Tsinghua University for providing computational and data storage resources that have contributed to the research results reported within this paper.

Software: pySIS (Albrow et al. 2009; Yang et al. 2024), OGLE DIA pipeline (Wozniak 2000), numpy (Harris et al. 2020), emcee (Goodman & Weare 2010; Foreman-Mackey et al. 2013), Matplotlib (Hunter 2007), and SciPy (Virtanen et al. 2020).

[20] This plateau still exists if we follow the criteria of Zang et al. (2024) to remove planets with large uncertainties in $\log q$.

ORCID iDs

Yuqian Gui https://orcid.org/0009-0007-9365-9806
Weicheng Zang https://orcid.org/0000-0001-6000-3463
Ruocheng Zhai https://orcid.org/0009-0004-1650-3494
Yoon-Hyun Ryu https://orcid.org/0000-0001-9823-2907
Andrzej Udalski https://orcid.org/0000-0001-5207-5619
Hongjing Yang https://orcid.org/0000-0003-0626-8465
Cheongho Han https://orcid.org/0000-0002-2641-9964
Shude Mao https://orcid.org/0000-0001-8317-2788
Michael D. Albrow https://orcid.org/0000-0003-3316-4012
Sun-Ju Chung https://orcid.org/0000-0001-6285-4528
Kyu-Ha Hwang https://orcid.org/0000-0002-9241-4117
Youn Kil Jung https://orcid.org/0000-0002-0314-6000
In-Gu Shin https://orcid.org/0000-0002-4355-9838
Yossi Shvartzvald https://orcid.org/0000-0003-1525-5041
Jennifer C. Yee https://orcid.org/0000-0001-9481-7123
Sang-Mok Cha https://orcid.org/0000-0002-7511-2950
Hyoun-Woo Kim https://orcid.org/0000-0001-8263-1006
Seung-Lee Kim https://orcid.org/0000-0003-0562-5643
Chung-Uk Lee https://orcid.org/0000-0003-0043-3925
Dong-Joo Lee https://orcid.org/0009-0000-5737-0908
Yongseok Lee https://orcid.org/0000-0001-7594-8072
Byeong-Gon Park https://orcid.org/0000-0002-6982-7722
Richard W. Pogge https://orcid.org/0000-0003-1435-3053
Przemek Mróz https://orcid.org/0000-0001-7016-1692
Michał K. Szymański https://orcid.org/0000-0002-0548-8995
Jan Skowron https://orcid.org/0000-0002-2335-1730
Radosław Poleski https://orcid.org/0000-0002-9245-6368
Igor Soszyński https://orcid.org/0000-0002-7777-0842
Paweł Pietrukowicz https://orcid.org/0000-0002-2339-5899
Szymon Kozłowski https://orcid.org/0000-0003-4084-880X
Krzysztof Ulaczyk https://orcid.org/0000-0001-6364-408X
Krzysztof A. Rybicki https://orcid.org/0000-0002-9326-9329
Patryk Iwanek https://orcid.org/0000-0002-6212-7221
Marcin Wrona https://orcid.org/0000-0002-3051-274X
Mariusz Gromadzki https://orcid.org/0000-0002-1650-1518
Renkun Kuang https://orcid.org/0000-0003-2337-0533
Wei Zhu https://orcid.org/0000-0003-4027-4711

References

Adams, A. D., Boyajian, T. S., & von Braun, K. 2018, MNRAS, 473, 3608
Alard, C., & Lupton, R. H. 1998, ApJ, 503, 325
Albrow, M. D., Horne, K., Bramich, D. M., et al. 2009, MNRAS, 397, 2099
Batista, V., Gould, A., Dieters, S., et al. 2011, A&A, 529, A102
Bennett, D. P., Bond, I. A., Abe, F., et al. 2017, AJ, 154, 68
Bennett, D. P., Bond, I. A., Udalski, A., et al. 2008, ApJ, 684, 663
Bennett, D. P., & Rhie, S. H. 1996, ApJ, 472, 660
Bennett, D. P., Rhie, S. H., Udalski, A., et al. 2016, AJ, 152, 125
Bensby, T., Yee, J. C., Feltzing, S., et al. 2013, A&A, 549, A147
Bozza, V. 2010, MNRAS, 408, 2188
Bozza, V., Bachelet, E., Bartolić, F., et al. 2018, MNRAS, 479, 5157
Calchi Novati, S., Skowron, J., Jung, Y. K., et al. 2018, AJ, 155, 261
Cassan, A., Kubas, D., Beaulieu, J. P., et al. 2012, Natur, 481, 167
Dong, S., Gould, A., Udalski, A., et al. 2009, ApJ, 695, 970
Foreman-Mackey, D., Hogg, D. W., Lang, D., & Goodman, J. 2013, PASP, 125, 306
Gaudi, B. S. 1998, ApJ, 506, 533
Gaudi, B. S. 2012, ARA&A, 50, 411
Gaudi, B. S., & Gould, A. 1997, ApJ, 486, 85

Gonzalez, O. A., Rejkuba, M., Zoccali, M., et al. 2012, A&A, 543, A13
Goodman, J., & Weare, J. 2010, CAMCOS, 5, 65
Gould, A. 1992, ApJ, 392, 442
Gould, A. 1994, ApJL, 421, L75
Gould, A. 1996, ApJ, 470, 201
Gould, A. 2000, ApJ, 542, 785
Gould, A. 2004, ApJ, 606, 319
Gould, A., Dong, S., Gaudi, B. S., et al. 2010, ApJ, 720, 1073
Gould, A., & Gaucherel, C. 1997, ApJ, 477, 580
Gould, A., Han, C., Zang, W., et al. 2022, A&A, 664, A13
Gould, A., & Loeb, A. 1992, ApJ, 396, 104
Gould, A., Udalski, A., Shin, I. G., et al. 2014, Sci, 345, 46
Han, C., Kim, D., Gould, A., et al. 2022, A&A, 664, A33
Han, C., Lee, C.-U., Udalski, A., et al. 2020, AJ, 159, 134
Han, C., Udalski, A., Kim, D., et al. 2021, A&A, 655, A21
Harris, C. R., Millman, K. J., van der Walt, S. J., et al. 2020, Natur, 585, 357
Holtzman, J. A., Watson, A. M., Baum, W. A., et al. 1998, AJ, 115, 1946
Hunter, J. D. 2007, CSE, 9, 90
Hwang, K.-H., Choi, J.-Y., Bond, I. A., et al. 2013, ApJ, 778, 55
Hwang, K.-H., Udalski, A., Shvartzvald, Y., et al. 2018, AJ, 155, 20
Hwang, K.-H., Zang, W., Gould, A., et al. 2022, AJ, 163, 43
Ida, S., & Lin, D. N. C. 2004, ApJ, 604, 388
Jiang, G., DePoy, D. L., Gal-Yam, A., et al. 2004, ApJ, 617, 1307
Jung, Y. K., Zang, W., Han, C., et al. 2022, AJ, 164, 262
Jung, Y. K., Zang, W., Wang, H., et al. 2023, AJ, 165, 226
Kennedy, G. M., & Kenyon, S. J. 2008, ApJ, 673, 502
Kim, D.-J., Kim, H.-W., Hwang, K.-H., et al. 2018, AJ, 155, 76
Kim, S.-L., Lee, C.-U., Park, B.-G., et al. 2016, JKAS, 49, 37
Kuang, R., Zang, W., Jung, Y. K., et al. 2022, MNRAS, 516, 1704
Mao, S. 2012, RAA, 12, 947
Mao, S., & Paczynski, B. 1991, ApJL, 374, L37
Mordasini, C., Alibert, Y., & Benz, W. 2009, A&A, 501, 1139
Nataf, D. M., Gould, A., Fouqué, P., et al. 2013, ApJ, 769, 88
Nemiroff, R. J., & Wickramasinghe, W. A. D. T. 1994, ApJL, 424, L21
Paczyński, B. 1986, ApJ, 304, 1
Park, B. G., DePoy, D. L., Gaudi, B. S., et al. 2004, ApJ, 609, 166
Poindexter, S., Afonso, C., Bennett, D. P., et al. 2005, ApJ, 633, 914
Poleski, R., Skowron, J., Udalski, A., et al. 2014, ApJ, 795, 42
Ranc, C., Bennett, D. P., Hirao, Y., et al. 2019, AJ, 157, 232
Ryu, Y.-H., Udalski, A., Yee, J. C., et al. 2024, AJ, 167, 88
Shin, I. G., Ryu, Y. H., Udalski, A., et al. 2016, JKAS, 49, 73
Shin, I. G., Ryu, Y. H., Yee, J. C., et al. 2019a, AJ, 157, 146
Shin, I. G., Yee, J. C., Gould, A., et al. 2019b, AJ, 158, 199
Shin, I.-G., Yee, J. C., Zang, W., et al. 2023, AJ, 166, 104
Shin, I.-G., Yee, J. C., Zang, W., et al. 2024, AJ, 167, 269
Shvartzvald, Y., Maoz, D., Udalski, A., et al. 2016, MNRAS, 457, 4089
Shvartzvald, Y., Yee, J. C., Skowron, J., et al. 2019, AJ, 157, 106
Skowron, J., Udalski, A., Gould, A., et al. 2011, ApJ, 738, 87
Suzuki, D., Bennett, D. P., Sumi, T., et al. 2016, ApJ, 833, 145
Szymański, M. K., Udalski, A., Soszyński, I., et al. 2011, AcA, 61, 83
Tomaney, A. B., & Crotts, A. P. S. 1996, AJ, 112, 2872
Udalski, A. 2003, AcA, 53, 291
Udalski, A., Jaroszyński, M., Paczyński, B., et al. 2005, ApJL, 628, L109
Udalski, A., Ryu, Y.-H., Sajadian, S., et al. 2018, AcA, 68, 1
Udalski, A., Szymanski, M., Kaluzny, J., et al. 1994, AcA, 44, 227
Udalski, A., Szymański, M. K., & Szymański, G. 2015, AcA, 65, 1
Virtanen, P., Gommers, R., Oliphant, T. E., et al. 2020, NatMe, 17, 261
Wang, H., Zang, W., Zhu, W., et al. 2022, MNRAS, 510, 1778
Wang, T., Calchi Novati, S., Udalski, A., et al. 2018, ApJ, 860, 25
Witt, H. J., & Mao, S. 1994, ApJ, 430, 505
Wozniak, P. R. 2000, AcA, 50, 421
Yang, H., Mao, S., Zang, W., & Zhang, X. 2021, MNRAS, 502, 5631
Yang, H., Yee, J. C., Hwang, K.-H., et al. 2024, MNRAS, 528, 11
Yang, H., Zhang, X., Hwang, K.-H., et al. 2020, AJ, 159, 98
Yee, J. C., Han, C., Gould, A., et al. 2014, ApJ, 790, 14
Yee, J. C., Shvartzvald, Y., Gal-Yam, A., et al. 2012, ApJ, 755, 102
Yee, J. C., Zang, W., Udalski, A., et al. 2021, AJ, 162, 180
Yoo, J., DePoy, D. L., Gal-Yam, A., et al. 2004, ApJ, 603, 139
Zang, W., Han, C., Kondo, I., et al. 2021a, RAA, 21, 239
Zang, W., Hwang, K.-H., Udalski, A., et al. 2021b, AJ, 162, 163
Zang, W., Jung, Y. K., Yang, H., et al. 2023, AJ, 165, 103
Zang, W., Jung, Y. K., Yee, J. C., et al. 2024, Sci, in press
Zang, W., Shvartzvald, Y., Udalski, A., et al. 2022a, MNRAS, 514, 5952
Zang, W., Yang, H., Han, C., et al. 2022b, MNRAS, 515, 928